Trace element geochemistry of sphalerite and chalcopyrite in arc-hosted VMS deposits

Lisard Torró, Diego Benites, Jean Vallance, Oscar Laurent, Brayam Ortiz-Benavente, Cyril Chelle-Michou, Joaquín Proenza, Lluís Fontboté

▶ **To cite this version:**

Lisard Torró, Diego Benites, Jean Vallance, Oscar Laurent, Brayam Ortiz-Benavente, et al.. Trace element geochemistry of sphalerite and chalcopyrite in arc-hosted VMS deposits. Journal of Geochemical Exploration, 2022, 232, pp.106882. 10.1016/j.gexplo.2021.106882 . hal-03436650

Trace element geochemistry of sphalerite and chalcopyrite in arc-hosted VMS deposits

Lisard Torró[a,*], Diego Benites[a], Jean Vallance[a], Oscar Laurent[b], Brayam A. Ortiz-Benavente[a], Cyril Chelle-Michou[b], Joaquín A. Proenza[c], Lluís Fontboté[d]

[a] *Geological Engineering Program, Faculty of Sciences and Engineering, Pontifical Catholic University of Peru (PUCP), Av. Universitaria 1801, San Miguel, Lima 15088, Peru*

[b] *Department of Earth Sciences, ETH Zürich, CH-8092 Zürich, Switzerland*

[c] *Departament de Mineralogia, Petrologia i Geologia Aplicada, Universitat de Barcelona (UB), Martí i Franquès s/n, 08028 Barcelona, Spain*

[d] *Department of Earth Sciences, University of Geneva, CH-1205 Geneva, Switzerland*

Submitted to *Journal of Geochemical Exploration*

[*] Corresponding author: Dr. Lisard Torró

E-mail address: lisardtorro@hotmail.com

Phone: (+51) 6262000 Ext. 5060

Abstract

Trace element compositions of sphalerite and chalcopyrite have been investigated for four arc-hosted Cretaceous VMS deposits (Palma, Perubar, and María Teresa in Peru, and Cerro de Maimón in the Dominican Republic) using laser ablation inductively-coupled plasma mass spectrometry. In sphalerite, Fe, Mn, Cd, Hg, Ag, Sb, Se, In, Ge, and Ga are lattice-bound, whereas Sn, Tl, Bi, and Pb occur at least partly as mineral microinclusions. Significant variations in the contents of minor and trace elements are observed in sphalerite grains from individual deposits. A strong negative correlation between Fe (Inter-Quartile Range [IQR] 44009-18168 ppm) and Zn indicates a dominant $Fe^{2+} \leftrightarrow Zn^{2+}$ simple isovalent substitution. Regarding potential *high-tech* by-products, the contents of In (IQR 42-1.6 ppm, up to 415 ppm) and Ga (IQR 31-5.9 ppm, up to 96 ppm) in the studied sphalerite are normally much higher than those of Ge (IQR 0.85-0.16 ppm, up to 9.3 ppm). Correlation trends suggest $Cu^{+} + In^{3+} \leftrightarrow 2Zn^{2+}$, $Cu^{+} + Ga^{3+} \leftrightarrow 2Zn^{2+}$, and additional, more complex substitution mechanisms of Zn involving combinations of monovalent (Cu^{+}, Ag^{+}), divalent (Ge^{2+}?), trivalent (In^{3+}, Ga^{3+}, [Sn^{3+}?]), and quadrivalent (Ge^{4+}, Sn^{4+}) cations.

As for chalcopyrite, Zn, Ag, Sn, Cd, Se, In, Ga, and Ge are interpreted to be lattice-bound, whereas Mo, Au, Tl, Sb, Pb, and Bi probably occur as microinclusions. Relative to sphalerite, chalcopyrite is depleted in In (IQR 28-8.4 ppm, up to 49 ppm) and Ga (IQR 8.3-2.9 ppm, up to 24 ppm) and enriched in Ge (IQR 5.9-0.70 ppm, up to 80 ppm). Of the other trace elements, Zn (IQR 426-190 ppm) is the most highly concentrated in the studied chalcopyrite, followed by Ag (IQR 136-23 ppm), Se (IQR 64-22 ppm), Sn (IQR 53-1.3 ppm), and Cd (IQR 12-6.0 ppm). General positive correlation trends between Zn, Cd, In, Ge, and Ga in chalcopyrite suggest varied coupled substitution mechanisms of Fe and Cu with fluctuating valences due to covalent bonding.

Trace-element distribution patterns in sphalerite and chalcopyrite were studied for the zone-refined Sofía-D massive sulfide body in the María Teresa deposit, which comprises a core of dominant pyrite sheathed outward with zones of chalcopyrite (Cu zone), sphalerite (Zn zone) and galena + sphalerite ± fahlore ± barite (Pb – Zn – Ag zone). Bottom to top of the sulfide body, sphalerite records progressive depletion in In, Cu, Mn, and Se, and enrichment in Ge. This distribution pattern agrees with increasing crystallization temperatures and/or volatile magmatic influx towards the core of the massive mineralization. Distribution of trace elements in chalcopyrite is rather uneven except for a sustained enrichment in Se towards the basal portion of the sulfide body. The fact that such trends are preserved in spite of extensive recrystallization during thermal metamorphism in parts of the Sofía-D massive sulfide mineralization suggests i) a closed metamorphic system and ii) that element interdiffusion was prominently local. Accordingly, we propose that sphalerite lattice-bound trace elements distribution patterns described in this article can help determine the polarity of massive sulfide bodies in VMS districts in metamorphosed and tectonized terranes.

Keywords: Sulfide; LA-ICP-MS; Coupled Substitution; Compositional Profile; Volcanic Arc; Latin America

1. Introduction

Volcanogenic massive sulfide (VMS) deposits are exhalative and/or replacive accumulations of sulfide minerals formed at or near the seafloor where uprising hydrothermal fluids driven by synchronous magmatism are entrained with cold seawater or porewaters (Doyle and Allen, 2003; Shanks and Thurston, 2012; Tornos et al., 2015). VMS mineralization occurs as sulfide mounds to tabular stratiform bodies, which are often underlain by a stockwork or feeder zone (Galley et al., 2007; Tornos et al., 2015). Their formation responds to the convergence in the time and space of anomalously high thermal gradients and extensional tectonic regimes that promote the circulation of evolved hydrothermal fluids through, and leaching of metals from, the oceanic strata (Ohmoto, 1996; Tivey, 2007; Piercey, 2011). Such geological features are primarily met in oceanic spreading ridges, arc environments, and rifted continental margins.

Most VMS deposits are preserved in suprasubduction zones either in back-arc, intra-arc, or forearc basins on both oceanic and continental crust (Franklin et al., 1998; Nimis et al., 2003; Herrington et al., 2005; Hollis et al., 2014; Peter et al., 2014; Torró et al., 2016a). In arc-related systems, contrasting water depths in massive sulfide formation exert a major control on the ore and hydrothermal alteration mineral assemblages and the metalliferous contents (Sillitoe et al., 1996; Dubé et al., 2007; Monecke et al., 2014). VMS deposits in back-arc and forearc basins form at water depths typically in the range between 1500 to 3700 m, whereas those in arc volcanoes and arc-related rifts are normally restricted to water depths in the range between 700 to 2000 m. The latter are often associated with elevated magmatic gas contents and boiling of the hydrothermal fluids may occur in shallower arc volcanoes and rifted intra-arc submarine hydrothermal systems (Gemmell et al., 2004; Dubé et al., 2007; Monecke et al., 2014).

VMS deposits are important sources of Cu, Zn, Pb, Au, and Ag (Galley et al., 2007). In addition, a wealth of other metals and metalloids that are potentially economically recoverable as byproducts (e.g., Sn, Co, Ni, In, Ga, Ge, Mo, Re, Se, Te) or deleterious (i.e., harmful or unwanted elements; e.g., Mn, As, Sb, Hg, Tl) may occur in remarkable concentrations in VMS deposits and even determine their economic viability (Benzaazoua et al., 2003; Zaccarini and Garuti, 2008; Koski and Mosier, 2012; Ridley, 2012; Carvalho et al., 2018; Frenzel et al., 2019). Minor and trace elements can either precipitate as native elements or substitute into the crystal lattice of major sulfide minerals (Cook et al., 2009, 2012, 2015; Ye et al., 2011; Ridley, 2012; Murakami and Ishihara, 2014; George et al., 2015, 2018; Benites et al., 2021a,b). The understanding of the mineralogical expression of either potential by-product or deleterious minor and trace elements in a given deposit or mineralization style is essential to predict their metallurgical behavior (e.g., Cook et al., 2011).

This study aims at understanding the mineralogical expression of minor and trace elements in sphalerite and chalcopyrite from arc-related VMS deposits and their distribution across massive sulfide bodies. To do so, we have systematically determined the trace element budget on these ore minerals from four arc-related VMS deposits in the Andes (Palma, Perubar, and María Teresa in Peru) and the Caribbean (Cerro de Maimón in the Dominican Republic). The obtained contents are compared with published data on other VMS deposits worldwide. In addition, a comprehensive set of samples has allowed the study of ore body-scale zoning of certain trace elements in a zone-refined massive sulfide body in the María Teresa deposit. The obtained results are used to assess the incorporation mechanisms of some *high-tech* elements to the crystal lattice of major sulfides (sphalerite and chalcopyrite) and contribute to revealing element distribution patterns across massive sulfide bodies in VMS districts; such patterns can be used to target the most prospective zones of zoned massive sulfide bodies for potential by-products and complementarily also to constrain sulfide body polarity during exploration in tectonized terranes.

2. Geological Setting

2.1. Volcanogenic massive sulfide deposits in Peru

2.1.1. General geologic framework

In Peru, several VMS deposits occur along the coastal region and are hosted by rocks of Cretaceous age (Steinmüller et al., 2000; Fontboté, 2019). In northern Peru, the giant Tambogrande deposits represent the largest VMS endowment in this country and probably in South America, and include the TG1 deposit with resources of 109 million metric tons (Mt) grading 1.6 % Cu, 1.0 % Zn, 0.5 g/t Au, and 22 g/t Ag, plus 16.7 Mt grading 3.5 g/t Au and 64 g/t Ag in oxide ore, and the TG3 deposit with resources of 82 Mt grading 1.0 % Cu, 1.4 % Zn, 0.8 g/t Au, and 25 g/t Ag (Manhattan Minerals, 2002 in Winter et al., 2010). There, VMS mineralization is hosted by subalkaline (calc-alkaline and tholeiitic) basaltic pillowed and brecciated lavas and lesser amounts of felsic volcanic rocks that filled N and NW-oriented sub-basins in the lower portion of the Lancones basin (Fig. 1; Tegart et al., 2000; Winter et al., 2004, 2010). The formation of the Lancones basin is connected to the break-up of Gondwana and coincided with a period of intense extension and rifting due to trench-rollback (Winter et al., 2010 and their references). Minimum age of massive sulfide formation (and likely synchronous with or slightly postdating massive sulfide formation) is constrained by U-Pb zircon dating of felsic volcaniclastic rocks at 104.8 ± 1.3 to 100.2 ± 0.5 Ma (middle Albian; Winter et al. 2010). The volcanic and sedimentary pile in the Lancones basin was intruded by Late Cretaceous to Tertiary arc-related granitoids of the Coastal Batholith (cf. Pitcher 1985; Atherton, 1990; Cobbing 1999; Hildebrand and Whalen, 2014).

In the central coastal segment of Peru, where the deposits studied in this paper are located, VMS mineralizations emplaced in the Huarmey and Cañete basins of the West Peruvian

Trough (WPT; Fig. 1) and are now exposed along the Peruvian Western Cordillera to the Coastal region. The opening of the WPT has been assigned to an aborted back-arc or true ocean floor extensional marginal basin (e.g., Atherton et al., 1985; Aguirre et al., 1989; Atherton and Aguirre, 1992) or to an intra-arc extensional pull-apart basin (Soler, 1991; Jaillard, 1994; Polliand et al., 2005, 2006). Stratigraphic relationships in the WPT led Scherrenberg et al. (2012) to delineate i) a western intra-arc basin, which is dominated by igneous rocks and that geographically coincides with the VMS mineralization; and ii) an eastern, deeper back-arc basin in which volcanic rocks overlie continental clastic rocks and marine carbonates. Major basin filling in the WPT occurred from latest Jurassic to Late Cretaceous (Mégard, 1984; Benavides-Cáceres, 1999). The stratigraphy of the WPT (at least in its western portion *sensu* Scherrenberg et al., 2012) is largely composed of a volcano-sedimentary sequence including bimodal mafic-felsic volcanic rocks, limestones, shales, sandstones, and local evaporites that was intruded by the Peruvian Coastal Batholith, which in part is coetaneous with the volcano-sedimentary sequence (Mégard, 1984; Atherton and Aguirre, 1992; Vela, 1997; Benavides-Cáceres, 1999; Polliand et al., 2005, 2006; Hildebrand and Whalen, 2014). The stratigraphy of the WPT is complex and includes abrupt lateral facies changes greatly limiting the stratigraphic correlation and age estimates of the sedimentary units. Since the scope of this article is limited to the geochemical composition of some ore minerals in selected VMS deposits, we will not elaborate on the nomenclature of hosting units but will simply conform with 'Casma Group' embracing the Albian-Cenomanian volcano-sedimentary sequence versus the younger 'Upper Cretaceous-Paleocene volcano-sedimentary sequence' (Romero et al., 2008; Cueva et al., 2010; Fontboté, 2019).

From north to south, the most representative VMS mineralization in the Huarmey and Cañete basins are the María Teresa, Aurora Augusta, Perubar, Palma, and Cerro Lindo (Fig. 1). Geochronology has given two groups of ages for these deposits: uppermost Cretaceous and mid-Cretaceous. High-resolution U-Pb zircon geochronology performed by Polliand et al. (2005) on rhyolitic lavas at the bottom and top of massive ore bodies in Perubar yields dates of 69.71 ± 0.18 and 68.92 ± 0.16 Ma, and on intrusive rocks, dates of 67.91 ± 0.17 and 67.89 ± 0.18 Ma. These dates ascribe the hosting rocks to the Upper Cretaceous-Paleocene volcano-sedimentary sequence and point to largely coeval subsidence, submarine volcanism, and plutonic activity within the Andean magmatic arc during the Late Cretaceous (Polliand et al., 2005; Polliand, 2006). At María Teresa, a date of 68 ± 6 Ma (Rb/Sr in hydrothermal sericite; Romero et al. 2008) points also to VMS mineralization in the latest Cretaceous. In contrast, the Cerro Lindo VMS mineralization is described to be hosted by a volcano-sedimentary sequence whose age has been attributed to the mid-Cretaceous (Casma Group) according to U-Pb zircon dating of host rhyolites at 105.7 ± 0.2 and 106.9 ± 0.2 Ma (Gariépy and Hinostroza, 2003; Votorantim, 2017; Bueno Carreón, 2019; Bueno Carreón and Mendoza Mondragón, 2019). Recent U-Pb zircon dating at 101 Ma of a diorite dike crosscutting the mineralization suggests that the Palma VMS deposit is also mid Cretaceous (Choquehuanca, 2020). At Aurora Augusta, hydrothermal sericite yielded inconclusive – both mid- and late Cretaceous – ages (K-Ar; Vidal, 1987).

Hydrothermal alteration in the María Teresa, Perubar, and Palma typically comprises intense sericite ± chlorite in the footwall and epidote + albite + chlorite + carbonates in the hanging wall and 'distal' domains of sulfide bodies (Fontboté, 2019). Sericite alteration is particularly well developed in the María Teresa deposit due to the exclusive igneous nature (i.e., plagioclase-rich) of the host rocks unlike in Perubar and Palma, where the presence of sedimentary rocks in the host sequence distorts the hydrothermal alteration halos. At María Teresa, the identification of a 'prospective horizon' outlined by an intense sericite alteration front has been interpreted as a paleo-horizon in which ascending hydrothermal fluids mixed with seawater in the volcanic pile in the sub-seafloor (Fontboté, 2019; Pichardo et al., 2019). Sulfur and Sr isotope data at Perubar support that mixing between a hydrothermal fluid (dominated by H_2S) and seawater triggered the mineralization (Polliand et al., 1999; Polliand, 2006). The setting of the María Teresa, Palma, and Perubar in a plutono-volcanic arc and the likely involvement of acidic-oxidizing fluids indicated by alteration and ore mineral assemblages are used by Fontboté (2019) to argue for a magmatic origin of the ore-forming hydrothermal fluids.

2.1.2. Geology of the María Teresa deposit

The Zn-Pb-Cu-Ag María Teresa mine is located 11 km NW of Huaral and 85 km N of Lima (Fig. 1) and is owned and operated by Minera Colquisiri SA since 1985.

Mineralization at María Teresa (>18 Mt high-grade Zn-Pb-Ag±Cu ore, Pichardo et al., 2019) occurs as replacement of volcanic and subvolcanic rocks that were intruded by a series of subvertical, N150E-oriented andesitic and dacitic dykes and, in places, by granodiorite and diorite plutons. Volcanic rocks at María Teresa comprise basaltic andesites and andesites and less abundant rhyodacites which, akin plutonic rocks in the district, show calc-alkaline affinity (Pichardo et al., 2019). Basaltic andesites and andesites show aphanitic, porphyritic textures drawn by plagioclase and amphibole phenocrysts. Amygdaloidal and brecciated textures are also common and, towards the upper section of the sequence, pillow lavas and hyaloclastites occur. Despite that the limit between individual lava flows is often blurred, the locally observed bedding is horizontal to slightly W-dipping. The N160E-oriented El Abra strike-slip fault dismembered and displaced clockwise the mineralization in the 'prospective horizon' so that the Calera sector has been displaced about 500 m to the south in relation to the Mine 2 and Bubulina sectors. In addition, the N140E-oriented Sofía reverse fault has slid the western block on top of the eastern block with an approximate vertical displacement of 90 m (Fig. 2). The mineralization in the María Teresa deposit occurs mostly as N150E-oriented irregular to lenticular massive sulfide bodies and underlying stockwork structures associated with abundant alteration to sericite and quartz (Pichardo et al., 2019). Close to the contact with granodiorite intrusions chiefly to the east of the Calera zone, a mineral assemblage including cordierite and garnet porphyroblasts along with biotite, phlogopite, and tremolite is interpreted as the contact metamorphic product of the hydrothermal sericite alteration (Pichardo et al., 2019). The ore mineralization includes sphalerite, chalcopyrite, tetrahedrite-group minerals, and galena, which occur along with variable proportions of pyrite ± pyrrhotite ± barite. The Sofía-D massive sulfide body is the largest in the deposit (~ 8 Mt grading 7.1% Zn, 1.37% Cu, 0.64% Pb, 60.3 g/t Ag; Pichardo et al., 2019) and shows clear metal zoning (Fig. 2). Metal zoning, ore mineral assemblages, and textures observed in this ore body are described in detail below. Due to the well-defined metal zoning in Sofía-D, it was selected in this study to trace the distribution of trace elements in sphalerite and chalcopyrite in zone-refined massive sulfide bodies.

2.1.3. Geology of the Perubar deposit

The Zn-Pb-Ba Perubar deposit is located 50 km E of Lima (Fig. 1) and was exploited between 1978 and 2000 with a production of 6 Mt with an average grade of 11.8% Zn and 1.4 % Pb (Polliand, 2006). The massive sulfide mineralization is hosted by an uppermost Cretaceous volcano-sedimentary sequence composed of submarine volcanic rocks and pyroclastic deposits of intermediate to felsic composition, intercalated with detrital sediments, volcaniclastic sandstones, tuffaceous mudstones, calcareous volcaniclastics, and limestones. Monzodiorite and monzogranite stocks belonging to the Coastal Batholith intruded in the area < ~1 Myr after the mineralizing event causing contact metamorphism at the Perubar deposit (Polliand et al., 1999; see Fig. 3 in Polliand et al., 2005; Polliand, 2006). The hydrothermal alteration of the host rocks comprises a siliceous core in the stockwork zone that grades outward to chlorite + pyrite ± sericite; extensive quartz + sericite developed in the footwall below the sulfide lenses, as well as distal quartz + K-feldspar. The deposit consists of four main massive barite-sulfide ore bodies (Graciela, Juanita, Cecilia Norte, and Cecilia Sur). According to Polliand (2006), the original (i.e., before tectonic deformation) ore zonation included a stockwork, which is now located north of the deposit, and massive mineralization that comprised pyrite(-magnetite) and pyrite-rich semi-black ores topped by a massive black ore, which graded laterally to banded barite-sulfide ores. The ore included pyrrhotite, pyrite, marcasite, magnetite, sphalerite, galena, barite, and lesser proportions of chalcopyrite, tetrahedrite, and arsenopyrite (Polliand, 2006). In addition, during our survey, tiny amounts of molybdenite and electrum were identified (Fig. S1). Representative photomicrographs of the samples containing the analyzed sphalerite from Perubar are shown in Figure S1. Polliand (2006) suggests that the conspicuously low proportion of chalcopyrite in the ore mineralization constrains the temperature of the mineralizing fluids < ~ 300 ºC.

2.1.4. Geology of the Palma deposit

The Zn-Pb Palma deposit is located 55 km SE of Lima and 15 km south of Perubar (Fig. 1). Ongoing exploration by Volcan Cía. Minera since 2009 has revealed a resource of 14.5 Mt including 9.6 Mt indicated at 5% Zn, 0.7% Pb, and 22 g Ag/t and 4.9 Mt inferred at 6% Zn, 1% Pb, and 21 g Ag/t, all reported with a cut-off of 3.5% Zn (Farfán et al., 2019). The mineralization is hosted in a volcano-sedimentary sequence consisting of sills and NNW-SSE trending dykes of basaltic to andesitic composition and local peperitic textures, organic matter-rich and framboidal-pyrite-bearing pelites, and shallow-water limestones. This sequence is cut by NNW-SSE-oriented felsic dykes. The igneous suite in the district displays calc-alkaline affinity (Farfán et al., 2019). Hydrothermal alteration includes deep, poorly developed sericite alteration and much widespread albite + epidote + chlorite + pyrite alteration The mineralization occurs as stacked massive sulfide bodies roughly parallel to the bedding and replaced chiefly limestone and subordinately pelitic and mafic and intermediate igneous rocks belonging to the lower section of the volcano-sedimentary sequence in the > 250-m-thick Palma Unit (see Fig. 3 in Farfán et al., 2019). Stringer and stockwork mineralization are also documented by these authors. Farfán et al. (2019) describe that the mineralogy of the upper semi-massive sulfide bodies comprises mainly pyrite, sphalerite, galena, and barite, with subordinate pyrrhotite and chalcopyrite, while the proportion of these two minerals increases in lower massive sulfide bodies. In addition, minor amounts of arsenopyrite and marcasite were identified during this survey. The samples analyzed in this work come from the upper semi-massive sulfide bodies. Representative microphotographs of samples containing the analyzed sphalerite from Palma are presented in Fig. S2. Ore and host rock have partly undergone contact metamorphism induced by arc plutons (Farfán et al., 2019).

2.2. Geology of the Cerro de Maimón deposit, Dominican Republic

The Cerro de Maimón VMS deposit is located 70 km northwest of Santo Domingo in central Dominican Republic (Fig. 3). It stands as the only VMS deposit currently under production in the Caribbean region. It is owned and operated by Perilya Limited through its subsidiary Corporación Minera Dominicana (CORMIDOM). The Cerro de Maimón massive sulfide body contains 4.8 Mt of proven and probable reserves grading 2.54% copper, 0.96 g/t Au, and 34.9 g/t Ag (Perilya, 2020). VMS mineralization and the metallogenic evolution of the Caribbean Greater Antilles are summarized and discussed by Nelson et al. (2011) and Torró et al. (2018a). The Cerro de Maimón massive sulfide mineralization is hosted by the Aptian Maimón Formation (Fig. 3), which is composed mostly of bimodal mafic-felsic volcanic and volcaniclastic rocks of boninitic and tholeiitic affinities emplaced in the forearc portion of the nascent Caribbean island-arc (Torró et al., 2016a, 2017, 2018b). Massive sulfides and hosting volcanic rocks were deformed and metamorphosed to peak metamorphic conditions in the greenschist/blueschist facies transition (Torró et al., 2016b). The mineralization is composed of pyrite grains with both cataclastic/blow-apart and metablastic welding textures and an interstitial assemblage of chalcopyrite + sphalerite + quartz + tennantite ± galena (paragenetic sequence and photomicrographs available in Fig. 6 in Torró et al., 2016a).

3. Materials and Methods

The study is based on 36 ore samples from the María Teresa (n = 24), Palma (n = 4), and Perubar (n = 5) deposits in Peru and the Cerro de Maimón deposit (n = 3) in the Dominican Republic. A list of the samples, their location, and brief textural descriptions are given in Table S1 in the Supplementary Material. In the María Teresa deposit, 15 ore samples picked up at different depths along a single drill core (34-18-S) that cut the zone-refined Sofía-D sulfide body (Calera sector) have been used to monitor mineralogical and mineral geochemical variations with depth. A total of 34 thick polished sections were produced at the QEMSCAN laboratory of the Pontificia Universidad Católica del Perú (PUCP) and examined using petrographic and scanning electron (SEM) microscopy. SEM images and major element mineral compositions were acquired on an environmental SEM Thermo Fisher Quanta 650 FEI equipment with an EDAX-Octane Pro EDS microanalysis system at PUCP (Centro de Caracterización de Materiales – CAM-PUCP) and a VEGA II XMU Tescan equipment with a Bruker QUANTAX EDS microanalysis system at BIZALAB at operating conditions of 5 nA and 20 kV accelerating voltage.

Minor and trace element compositions of sphalerite and chalcopyrite were determined by means of electron microprobe (EPMA), at the University of Barcelona, and laser-ablation inductively-coupled plasma mass spectrometry (LA-ICP-MS), at the ETH Zürich, using the same equipment and methodology as described in Benites et al. (2021a). For samples from the María Teresa, Palma, and Perubar deposits, representative EPMA analyses of sphalerite and chalcopyrite are displayed in Table S2 in Supplementary Material. For samples from the Cerro de Maimón deposit, representative EPMA analyses of sulfide minerals are provided in Torró et al. (2016a). LA-ICPMS data are reported in Table S3 in Supplementary Material. Content statistical data for sphalerite and chalcopyrite are shown in Tables 1-2.

4. Results

4.1. Ore mineral geochemistry

Major and trace element compositions of sphalerite and chalcopyrite show, in general, a wide range of elements at measurable contents. Summaries of their compositions, including minimum, maximum, geometric mean, standard deviation, and interquartile range (IQR) values are displayed in Tables 1 and 2. Content values will be hereinafter reported as IQR unless otherwise specified. Significant effort was made to report only the content of elements whose variations respond to solid solutions and not to mixed mineral analyses by analyzing mineral volumes free of obvious inclusions and by selecting only stable signal intervals in LA-ICP-MS spectra (Fig. S3 in Supplementary Material). However, it should be noted that evenly distributed nano-inclusions may also yield flat ablation profiles (e.g., Gregory et al., 2015) and that, therefore, the possibility of mixed mineral analyses cannot be completely discarded due to the relatively low spatial resolution of the used methods.

4.1.1. Sphalerite

Iron, Mn, Cd, Hg, and Cu (Fig. S3 in Supplementary Material) yield smooth and constant ablation profiles. Studied sphalerite shows a relatively wide range of Fe contents in samples from the María Teresa deposit (40675-17122 ppm), which are higher than in samples from the Cerro de Maimón (585-535 ppm) and generally lower than in samples from the Perubar (67570-39965 ppm) and Palma (63423-30015 ppm) deposits (Table 1). Manganese also shows a relatively wide range of contents in sphalerite from María Teresa (2343-326 ppm), which overlaps with the composition of grains from Cerro de Maimón (482-446 ppm) and are in general lower than in grains from Perubar (5964-907 ppm) and Palma (7751-6734 ppm). The contents of Cd are constantly high in all analyzed sphalerite samples (7373-5290 ppm in María Teresa, 6665-4297 ppm in Perubar, 7109-4782 ppm in Palma, and 3829-3574 ppm in Cerro de Maimón). Mercury contents are higher in sphalerite from the Palma (667-593 ppm) and María Teresa (448-326 ppm) deposits than in sphalerite from the Perubar (107-18 ppm) and Cerro de Maimón (26-22 ppm) deposits. The content of Cu is generally higher in sphalerite samples from the Cerro de Maimón (138-113 ppm) and María Teresa

(98-36 ppm) deposits than in sphalerite samples from the Perubar (41-25 ppm) and Palma (31-11 ppm) deposits.

At generally lower contents and also showing smooth ablation spectra are Ag, In, Ge, and Ga (Table 1; Fig. S3 in Supplementary Material). Silver content ranges mostly overlap in sphalerite grains from the four studied deposits (12-4.2 ppm in María Teresa, 7.1-3.6 ppm in Perubar, 17-3.8 ppm in Palma, and 4.2-3.1 ppm in Cerro de Maimón). The contents of In are in general much higher in sphalerite from the María Teresa deposit (68-4.4 ppm, up to 415 ppm) than in sphalerite from the Cerro Maimón (10-9.5 ppm), Perubar (2.3-0.78 ppm) and Palma (0.22-0.0091 ppm; Table 1) deposits. Gallium contents are higher in sphalerite from the Cerro de Maimón deposit (95-78 ppm, up to 96 ppm) than in sphalerite from the María Teresa (32-11 ppm, up to 94 ppm), Perubar (30-4.7ppm), and Palma (2.4-1.9 ppm) deposits. Germanium contents are in general very low in analyzed sphalerite grains (0.65-0.17 ppm in María Teresa, 0.19-0.15 ppm in Perubar, 3.5-0.16 ppm in Palma, and 1.2-0.68 ppm in Cerro de Maimón).

The content of other elements are in general very low (Pb: 9.3-1.1 ppm; Sb: 3.7-0.31 ppm; Tl: 0.66-0.045; Sn: 0.49-0.23 ppm; Bi: 0.60-0.0055 ppm; detailed results for individual deposits are available in Table 1). Some analyses show slightly ragged ablation spectra (Fig. S1 in Supplementary Material).

4.1.2. Chalcopyrite

Chalcopyrite grains from the María Teresa and Cerro de Maimón VMS deposits have been analyzed. Zinc, Ag, Sn, Cd, Se, In, Ge, and Ga show relatively constant ablation profiles (Fig. S3 in Supplementary Material). Zinc is the trace element most highly concentrated in studied sphalerite grains; its contents are higher in chalcopyrite from the María Teresa deposit (425-194 ppm) than in chalcopyrite from the Cerro de Maimón deposit (a single analysis >d.l. yields a concentration of 71 ppm; Table 2). Silver, Sn, and Cd are relatively enriched in chalcopyrite grains from the María Teresa deposit (150-71 ppm Ag, 77-33 ppm Sn, 12-6.2 ppm Cd) relative to grains from the Cerro de Maimón deposit (23-15 ppm Ag, 1.6-1.4 ppm Sn, 0.53-0.41 ppm Cd). Selenium is more concentrated in chalcopyrite from the Cerro de Maimón deposit (89-79 ppm) than in chalcopyrite from the María Teresa deposit (31-19 ppm). Indium values are relatively constant in analyzed grains from the studied deposits and are systematically higher in chalcopyrite from María Teresa (32-12 ppm) than in chalcopyrite from Cerro de Maimón (8.1-7.3 ppm). The contents of Ga and Ge are in general lower than those of In (9.2-2.6 ppm Ga and 4.3-0.66 ppm Ge in María Teresa; 3.6-3.3 ppm Ga and 6.1-5.3 ppm Ge in Cerro de Maimón).

Downhole ablation spectra reveal very irregular profiles for Mo and Au and in some samples, slightly irregular profiles for Tl, Sb, and Bi (Fig. S3 in Supplementary Material). Molybdenum yields relatively erratic contents, which are much higher in analyzed chalcopyrite from Cerro de Maimón (83-23 ppm) than in chalcopyrite from María Teresa (0.034-0.021 ppm, and mostly <d.l.). The contents of Tl (< 11 ppm), Sb (< 31 ppm), Bi (< 10 ppm), and Au (< 0.40 ppm) are relatively low (Table 2).

4.2. Metal zonation, mineralogy and trace-element distribution patterns in the zone-refined Sofía-D body

The metal zonation in Sofía-D massive sulfide body includes, bottom to top, i) a Cu zone composed dominantly of chalcopyrite and lesser amounts of sphalerite grading downward to massive pyrite; ii) a Zn zone in which sphalerite is the most abundant phase and appears along with lesser amounts of galena and chalcopyrite and minor fahlore; and iii) a Pb – Zn – Ag zone with abundant galena and sphalerite, and lesser proportions of fahlore and barite (Fig. 2).

On the hand sample scale, sphalerite occurs as mm- to cm-sized grains of yellow-pale brown (Fig. 4A-C) and red-brownish (Fig. 4D-E) color. In places, the massive sphalerite aggregates are cut by irregular, chalcopyrite-rich veinlets (Fig.4A, D-E). In the eastern part of the María Teresa deposit, i.e., close to the granodiorite stock as is the case for the Sofia D ore body, coarse-grained pyrrhotite ± magnetite is observed and, similarly to in Perubar (see Vidal, 1987; Polliand et al., 1999), interpreted as the metamorphic product after pyrite. An example is shown in Figure 4F coming from a 20-cm-wide band composed of coarse-grained pyrrhotite ± magnetite at the contact with and andesitic dyke. In volcaniclastic rocks in the immediate host of the Sofía-D body, chalcopyrite selectively replaced some of the clasts and the matrix (Fig. 4G). Silicified dykes that cut the Sofía-D body typically contain patches and irregular veinlets of chalcopyrite (Fig. 4H).

Under the petrographic microscope, pyrite grains, which have sizes typically in the range between 100 and 600 µm, draw a variety of textures including anhedral isolated grains with roundish and embayed outlines, aggregates of several grains often with foam equilibrium textures (i.e., contacts at 120º) and, in some cases, internal irregular fractures (Fig. 5A-D). Arsenopyrite is relatively scarce in the studied samples and appears as isolated euhedral and subhedral fractured grains and sizes in the range between 50 and 200 µm (Fig. 5C-D). The other sulfides, fahlore (tennantite-(Fe) ± argentian tetrahedrite), and traces of other sulfosalts such as bournonite, boulangerite, and polybasite (petrographic observations complemented with EDS analyses) occupy interstitial space between, and line porosity and fractures within, pyrite ± arsenopyrite grains (Fig. 5). According to these observations, pyrite and arsenopyrite crystallized early in the paragenetic sequence (Fig. 6) and, in places, underwent thermal re-equilibration connected to dyke and granodiorite intrusions (Pichardo et al., 2019). Internal fractures of pyrite and arsenopyrite (Fig. 5C) also point to fragile deformation, probably due to movements along the Sofía reverse fault (Fig. 2). Sphalerite grains in the Zn zone show clean surfaces (Fig. 5B,E), whereas in the Cu zone they have been pervasively replaced by chalcopyrite and show dense chalcopyrite disease textures (Fig. 5D, F-G). Chalcopyrite floods the interstitial space between pyrite ± arsenopyrite in the Cu zone along with relicts of sphalerite and in places shows sharply bounded exsolutions of cubanite laths up to 150 µm in length (Fig. 5G). Auriferous silver (73 wt.% Ag, 27 wt.% Au, EDS analysis) has been observed in one sample and appears as minute grains (< 2 µm) in fractured arsenopyrite along with chalcopyrite (Fig. 5H).

The systematic sampling developed along the drill core 34-18-S from 72.85 to 128 m (Table S1 in the Supplementary Material) allows for the assessment of vertical trends in trace-element contents in sphalerite and chalcopyrite. Bottom to top in sphalerite, there is a relatively sustained decrease in the contents of Mn, Cu, Se, Bi, and In and an increase of Ge, and the contents of elements such as Cd and Ga show irregular distributions (Fig. 7A-G). The contents of In significantly decrease from sample 2019-MT-015 (128 m, 167-158 ppm) to sample 2019-MT-001 (72.85 m, 4.4-4.1 ppm), although the maximum contents occur in sample 2019-MT-004 (81.4 m, 409-399 ppm; Fig. 7G). The distribution of Cu contents almost mimics that of In, with a decrease from sample 2019-MT-015 (128 m, 203-160 ppm) to sample 2019-MT-001 (72.85 m, 27-24 ppm), although with maximum contents at intermediate depths in samples 2019-MT-004 (81.4 m, 335-321 ppm) and 2019-MT-011 (105.5 m, 597-115 ppm; Fig. 7C). Germanium contents show a moderately irregular distribution pattern with a general increase in its content from sample 2019-MT-015 (128 m, 0.33-0.23 ppm) to sample 2019-MT-002 (74.6 m, 1.3-0.73 ppm; Fig. 7I). As for chalcopyrite, vertical distribution patterns are mostly irregular (Fig. 8). The most remarkable exception is Se, which content tends to decrease steadily at shallower levels (45 ppm – single value – in sample 2019-MT-015 at 128 m, 31-27 ppm in sample 2019-MT-012 at 109.4 m, 11-10 ppm in sample 2019-MT-007 at 90.5 m; Fig. 8E). An opposite trend is defined by the content of Ge, with general enrichment from deeper (2.2 ppm – single value – in sample 2019-MT-015 at 128 m, 0.84-0.60 ppm in sample 2019-MT-012 at 109.4 m,) to shallower (80-74 ppm in sample 2019-MT-007at 90.5 m) chalcopyrite samples (Fig. 8J). Although probably hosted as sub-microscopic mineral inclusions, the content of Bi in chalcopyrite also shows significant variation and tends to increase with depth (Fig. 8G).

5. Discussion

5.1. Trace-element budget in sphalerite and chalcopyrite from arc-hosted VMS deposits

The minor and trace element contents measured in sphalerite and chalcopyrite from the Palma, Perubar, María Teresa (Perú), and Cerro de Maimón (Dominican Republic) VMS deposits will be compared along the following lines with available data from other VMS deposits, and particularly with those formed in arc systems. We have compared our results with the comprehensive compilation by Monecke et al. (2014) of whole-rock and mineral geochemical data from both active seafloor massive sulfide (SMS) and fossil equivalent deposits emplaced in a variety of tectonic settings worldwide.

Sphalerite from the four investigated deposits yields fairly variable Fe contents (Table 1), the content of the other analyzed trace elements being largely subordinated to that of Fe. The content of Fe in sphalerite samples from the Cerro de Maimón deposit analyzed in this study is particularly low (Table 1); a more complete geochemical dataset based on EPMA analyses on sphalerite samples from this deposit reported by Torró et al. (2016a) indicates average Fe contents of 1.16 wt.%. Iron contents in the studied deposits are compatible with sphalerite crystallized in intermediate to high-intermediate sulfidation environments in equilibrium with pyrite (Barton and Toulmin 1964; Hannington and Scott, 1989). Co-crystallization of fahlore (tennantite and tetrahedrite) along with sphalerite in the studied ore samples is a further indication of intermediate-sulfidation state of the hydrothermal mineralizing fluids. Similar Fe contents to those in the studied Andean VMS deposits are reported in sphalerite samples from the Zinkgruvan, Marketorp, and Sauda VMS deposit (Table 3 and references therein). Iron contents similar to those found in sphalerite from the Cerro de Maimón deposit are reported in the Vorta, Eskay Creek, and Çayeli VMS deposits. In contrast, sphalerite from the VMS Laochang deposit (South China) systematically yields higher Fe contents.

The relatively high content of Cd in sphalerite from the studied deposits (Table 1) are comparable with those in sphalerite from other VMS deposits such as Vorta, Eskay Creek, Zinkgruvan, Marketorp, and Laochang, and higher than in Sauda (Table 3). Cadmium contents of several hundreds of parts per million are typical of SMS emplaced in arc settings compared to contents in the range of some tens of parts per million in those emplaced in mid-ocean ridge systems, sphalerite and wurtzite bein the main Cd hosts in VMS deposits according to Monecke et al. (2014). According to our (Table 1) and previous (Table 3) data, Cd in sphalerite from VMS deposits in arc systems typically yields contents of several thousands of parts per million. The content of Hg varies between some tens (Perubar and Cerro de Maimón) and some hundreds (María Teresa and Palma) of parts per million in the studied sphalerite samples; the content of Hg is not provided for sphalerite from other VMS deposits in arc systems in the revised literature. Petersen et al. (2014) reported contents between <0.02 and 7.4 wt.% Hg (median = 0.37 wt.% Hg; EPMA data) in sphalerite from the Palinuro SMS deposit in the Aeolian arc (transitional arc setting). Monecke et al. (2014) found out that the content of Hg in SMS is higher in mineralization emplaced in arc volcanoes and rifted arcs (some tens of ppm) relative to mineralization emplaced in back-arc spreading centers and mid-ocean ridges; also, that Hg usually shows a strong positive correlation with Sb in mineralized samples from SMS which normally results from the chief concentration of Hg in tetrahedrite and tennantite over other ore minerals. The contents of

Sb in the studied sphalerite are mostly in the 1-10 parts per million range or below (Table 1), similar to sphalerite from other VMS mineralization such as Vorta, Zinkgruvan, and Laochang, and lower than in Eskay Creek and Çayeli (Table 3). The content of Tl in the studied sphalerite samples is normally below 1 ppm (Table 1), similar to sphalerite from other VMS deposits with the exception of Çayeli, in which the content of Tl is much higher (13-4.9 ppm; Table 3). The contents of Sb and Tl are usually higher in sulfide samples from SMS mineralization emplaced in arc volcanoes and rifted arcs than in SMS mineralization emplaced in back-arc spreading centers and mid-ocean ridges according to data compiled by Monecke et al. (2014).

The studied sphalerite samples yield In contents largely in the range between <1 ppm and some tens of parts per million (Table 1), similar to sphalerite from Vorta, Eskay Creek, Zinggruvan, Marketorp, and Sauda, and lower than in Laochang (Table 3). The measured In contents are also much lower than in sphalerite from the Neves Corvo VMS deposit (up to 2.1 wt.%, EPMA data: Carvalho et al., 2018). The contents of Ga in the sphalerite samples analyzed here are largely of the same order of magnitude (from a few ppm to ~100 ppm) as contents reported for sphalerite from other VMS deposits (Table 3), whereas the contents of Ge (mostly <1 ppm) are generally lower than those reported in the literature. The contents of In, Ge, and Ga are mostly indistinguishably low in SMS sulfides irrespective of their tectonic environment of emplacement (Monecke et al., 2014).

In the studied chalcopyrite samples from the Andean VMS deposits, the content of Zn is of some hundreds of parts per million (Table 2), similar to chalcopyrite from Vorta, Sulitjelma, and Kutlular, and lower than in chalcopyrite from Çayeli (Table 4 and references therein); Zn content in sphalerite from the Cerro de Maimón deposit is significantly lower. The contents of Ag are mostly in the range between a few to some hundreds of parts per million in the analyzed chalcopyrite (Table 2), like chalcopyrite from VMS reported in the literature (Table 4). Selenium contents in the studied chalcopyrite samples are of some tens of parts per million (Table 2), and therefore lower than Se contents in chalcopyrite from other subduction-related VMS deposits, which are mostly in the hundreds of parts per million range (Table 4). According to Monecke et al. (2014), chalcopyrite is the main host of Se in VMS and SMS deposits along with pyrite and, typically, higher Se contents are found in sulfide samples collected in SMS formed in mid-ocean ridges relative to those in subduction related systems. Cadmium shows contents of a few to some tens of parts per million in the analyzed chalcopyrite samples (Table 2), similar to chalcopyrite from other VMS deposits (Table 4); therefore, as expected, Cd contents are much lower in chalcopyrite than in sphalerite from the same deposit (Tables 1 and 3). Similarly, Hg contents in chalcopyrite (up to a few ppm, Table 2) are much lower than in sphalerite (Table 1) from the respective deposits, and similar to or slightly higher than Hg content in chalcopyrite from the Vorta and Sulitjelma VMS deposits (Table 4).

Indium content in analyzed chalcopyrite grains, mostly at the level of tens of parts per million, is only slightly lower than In content in sphalerite grains from the same deposits (Tables 1 and 2), and steadily higher than in chalcopyrite grains from the Vorta and Sulitjelma VMS deposits (Table 4). Germanium content in the analyzed chalcopyrite samples is mostly at the level of some parts per million (Table 2) and usually higher than in sphalerite from the respective deposits (Table 1); Ge content is not provided in reference data for chalcopyrite from other VMS deposits (Table 4). The content of Ga (mostly at the level of a few ppm to some tens of ppm) is lower in chalcopyrite than in sphalerite from the same deposit (Tables 1 and 2); the content of Ga in chalcopyrite from the Vorta and Sulitjelma VMS deposits is systematically lower than in the samples analyzed here (Table 4).

5.2. Correlation trends and substitution mechanisms

5.2.1. Sphalerite

The dataset shows a marked negative correlation trend between Fe and Zn with a slope of ~1 (Fig. 9A) that indicates a dominant $Fe^{2+} \leftrightarrow Zn^{2+}$ simple isovalent substitution. Fair positive correlations between Ag and both Pb (Fig. 9B) and Sb (Fig. 9C) suggest that these three elements likely occur in solid solution in the studied sphalerite samples. Tin is also positively correlated with Ag and the reasonable positive correlation in the Sb+Sn vs. Ag+Pb plot (Fig. 9D) with a slope ~1 suggests incorporation of these elements via coupled substitutions of the type $Ag^{+} + Pb^{2+} + (Sn,Sb)^{3+} \leftrightarrow 3Zn^{2+}$ and likely also via independent variations of this scheme (Cook et al., 2009). Nevertheless, the observation of slight ragged downhole ablation spectra for Sn and Pb in a few analyses (e.g., Fig. S3D in Supplementary Material) might suggest the local presence of sub-microscopic inclusions of galena and/or Sn-Pb sulfosalts.

The dataset shows a marked correlation trend between Cu and In in samples from María Teresa, particularly in those with the highest In contents, with a slope ~1 (Fig. 10A) thus pointing to a $Cu^{+} + In^{3+} \leftrightarrow 2Zn^{2+}$ coupled substitution (Cook et al., 2012; Trofimov et al., 2020; Benites et al., 2021a,b). Gallium yields a fair positive correlation with Cu with some analyses plotting along or close to the 1:1 correlation line (Fig. 10B) suggesting a $Cu^{+} + Ga^{3+} \leftrightarrow 2Zn^{2+}$ coupled substitution. Germanium contents do not show clear correlation trends with the other analyzed elements. The alignment of the analyses in the Sn+In+Ge+Ga vs. Cu + Ag plot (R = 0.55; Fig. 10C) would suggest supplementary complex substitution mechanisms involving combinations of coupled substitutions of trivalent cations (i.e., In, Ga) with monovalent cations (i.e., Cu, Ag) and direct substitution of quadrivalent cations (Sn, Ge) with vacancies for Zn. However, the lacking consensus on the oxidation state of Ge (+2 or +4) and Sn (+3 or +4) in sphalerite leaves open the possibility of other substitution schemes (see Cook et al., 2009, 2015; Bellisont et al., 2014). The low content of both Sn and Ge in the studied sphalerite grains and the apparent lack of individual correlation trends with other analyzed elements do not allow to give a definitive conclusion on their incorporation in the crystal lattice.

5.2.2. Chalcopyrite

Unlike sphalerite, chalcopyrite is not a fully ionic mineral but bonding between atoms in its structure is “effectively” covalent with valencies of Fe fluctuating between divalent and trivalent and valencies of Cu, between monovalent and divalent (Donnay et al., 1958; Hall and Stewart, 1973; Li et al., 2013). Therefore, the incorporation mechanism of trace elements in chalcopyrite is far more complex to draw than for sphalerite (see George et al., 2018). Weak to fair positive correlation trends between Zn, Cd, In, Ge, and Ga are observed across our dataset (Fig. 11). George et al. (2018) also noticed the positive correlation between Zn and Cd in chalcopyrite samples from a variety of mineralization styles and argued that systematic variations of Cd:Zn ratio are strongly dependent on crystallization temperature (this question is further addressed in the following section). Our data would suggest that the incorporation of Zn, Cd, In, Ge, and Ga to the structure of chalcopyrite is not completely independent (i.e., simple substitution) but that coupled substitutions involving cations of these elements are likely (see also George et al., 2018 and their references).

5.3. Trace element distribution profiles and conditions of crystallization (and re-crystallization)

Metal and mineral zonation (Fig. 2) and the overprinting and replacement of earlier sulfides (e.g., sphalerite) by minerals that are stable at higher temperature (e.g., chalcopyrite; Figs. 4-6) as described for Sofía-D in the María Teresa deposit denote a thermally intensifying hydrothermal system during the growth of the massive sulfide body; in VMS systems, this process is commonly known as zone refining (Eldridge et al., 1983; Hannington et al., 1998; Grant et al., 2015; Almodóvar et al. 2019). According to the GGIMFIS geothermometer of Frenzel et al. (2016) – which uses the contents of Fe, Mn, In, Ga, and Ge in sphalerite, the analyzed sphalerite from the María Teresa deposit crystallized at temperatures in the range between 320 and 257 ºC (IQR). Such a temperature range is in good agreement with a VMS mineralization containing fair abundant chalcopyrite (Hannington et al., 1995; Ohmoto, 1996; Franklin et al., 2005). Assuming that fO_2 and fS_2 were stable during the crystallization of sphalerite (see Hannington and Scott, 1989 and Keith et al. 2014) in the Sofía-D sulfide body, sphalerite composition would record a relatively sustained decrease in the crystallization temperature bottom to top (335-327 ºC for sample 2019-MT-015 at 128 m to 255-249 ºC for sample 2019-MT-002 at 74.6 m; Fig. 7J). This decrease in the calculated crystallization temperature is actually a numerical translation of the depletion in In and Mn (directly proportional to the GGIMFIS temperature) and the enrichment in Ge (inversely proportional to the GGIMFIS temperature) bottom to top in sphalerite of the Sofía-D massive sulfide body (Fig. 7). Noteworthy, an increase in the availability of Cu in the mineralizing fluid towards the Cu zone probably also enhanced the incorporation of In to the sphalerite crystal lattice through the coupled substitution mentioned above ($Cu^{+} + In^{3+} \leftrightarrow 2Zn^{2+}$) during zone refining processes.

The Cd:Zn ratio in chalcopyrite is commonly used to trace variations in physicochemical conditions during its crystallization. Higher Cd:Zn ratios are typically ascribed to higher temperatures of crystallization (George et al. 2018). In the Sofía-D sulfide body, chalcopyrite shows rather constant Cd:Zn ratios at different depths and sections (Fig. 8K) suggesting relatively homogeneous physicochemical conditions during the crystallization of this mineral throughout the Cu zone of the mineralized body (Fig 2). In contrast, the increase of Se contents in chalcopyrite (and sphalerite) with depth would suggest an increase in the temperature and/or magmatic volatile influx (Auclair et al., 1987; Huston et al., 1995; Layton-Matthews et al., 2008; Martin et al. 2019). The concentration of Se, and most trace elements indeed, in the structure of chalcopyrite is distinguishingly strongly influenced by the co-crystallizing phases so that the continuous crystallization of galena during zone refining probably partitioned Se and depleted chalcopyrite in this element (Cook, 1996; Carvalho et al., 2018; George et al. 2018). The progressively increasing abundance of galena towards the upper sections of the Sofía-D body may therefore explain the progressive depletion of Se in chalcopyrite at shallower levels.

In short, our results suggest that in zone-refined VMS mineralization such as the Sofía-D massive sulfide body in the María Teresa deposit, chalcopyrite and particularly sphalerite register systematic changes in their trace element compositions across the mineralized body. Bottom to top of the sulfide body, observed trends include i) in sphalerite, depletion in In, Cu, Mn, Se, and Bi and enrichment in Ge; and ii) in chalcopyrite, depletion in Se and Bi (the latter probably in microinclusions). Furthermore, these patterns agree with expected physicochemical trends involving decreasing temperatures and influx of hydrothermal fluids with a direct magmatic contribution towards the margins of the sulfide body (Auclair et al., 1987; Huston et al., 1995; Layton-Matthews et al., 2008; Yeats et al., 2014; George et al. 2018; Schmidt et al., 2018; Martin et al. 2019).

Ore mineralization at the Sofía-D massive sulfide body in the María Teresa deposit underwent contact metamorphism connected to nearby granodiorite intrusions (Fig. 2). The identification of key trace-element distribution patterns in sphalerite and chalcopyrite across this body and their reconciliation with expected original trends suggest that contact metamorphism occurred in a closed system and more importantly, that body-scale trace element distribution was largely unaffected. Similarly, Polliand et al. (1999) determined that in the Perubar VMS deposit, sulfur isotope re-equilibration between sulfate-sulfide pairs during contact metamorphism occurred in a closed system and only between adjacent mineral grains. Lockington et al. (2014) found out that the content of lattice-bound trace elements in sphalerite (e.g., Mn, Fe, Cd, Cu, In, Ge, Hg, and Se) from metamorphosed VMS deposits worldwide showed no correlation with the metamorphic grade but were defined primarily by physicochemical conditions during initial deposition; in contrast, the contents of elements that typically occur as micro- and nano-inclusions in sphalerite (e.g., Pb and Bi) decreased with increasing metamorphic grade. Therefore, the use of trace element patterns defined by Mn, In, Ge, and Se in sphalerite, and of Se in chalcopyrite, are likely to reflect primary trends.

6. Conclusions and implications

In this study, systematic trace element determinations have been conducted in sphalerite and chalcopyrite from the Cretaceous arc-related Palma, Perubar, and María Teresa VMS deposits in Peru and the Cerro de Maimón VMS deposits in the Dominican Republic. Sphalerite from the four deposits incorporated Fe, Mn, Cd, Hg, Ag, Sb, Se, In, Ge, and Ga in solid solution. The incorporation of other elements such as Sn, Tl, Bi, and Pb possibly resulted in some cases from microinclusions as suggested by occasional ragged ablation spectra. The contents of minor and trace elements in analyzed sphalerite show significant variations even between samples from any individual deposit. Iron contents (44009-18168 ppm) correlate negatively with Zn suggesting a dominant $Fe^{2+} \leftrightarrow Zn^{2+}$ simple isovalent substitution. Cadmium (7082- 4972 ppm), Mn (4578-140 ppm), and Hg (453-107 ppm) are much concentrated than Pb (9.5-1.1 ppm), Sb (3.7-0.31 ppm), Tl (0.70-0.045 ppm), and Bi (0.60-0.0055 ppm).

Regarding potential *high-tech* by-products in the studied sphalerite grains, In (42-1.6 ppm, up to 415 ppm) and Ga (31-5.9 ppm, up to 96 ppm) contents are mostly higher than Ge contents (0.85-0.16 ppm, up to 9.3 ppm). In samples from the María Teresa deposit, the concentrations of In and Cu yield a positive correlation trend with a slope ~1 corroborating a $Cu^{+} + In^{3+} \leftrightarrow 2Zn^{2+}$ coupled substitution. The dataset also shows a positive correlation trend between Ga and Cu; analyses of sphalerite from the María Teresa, Perubar and Cerro de Maimón deposits lie close to the Ga:Cu 1:1 ratio line thus pointing to a $Cu^+ + Ga^{3+} \leftrightarrow 2Zn^{2+}$ coupled substitution. Furthermore, the narrow arrangement of most analyses along the 1:1 ratio line in a In + Ga + Ge + Sn vs. Cu + Ag plot suggests the occurrence of additional, more complex substitution mechanisms involving different combinations of monovalent (Cu^+, Ag^+), divalent (Ge^{2+}?), trivalent (In^{3+}, Ga^{3+}, [Sn^{3+}?]), and quadrivalent (Ge^{4+}, Sn^{4+}) cations.

The trace element composition of chalcopyrite was investigated for the María Teresa and Cerro de Maimón deposits as chalcopyrite is a trace phase in the Palma and Perubar deposits. Trace elements such as Zn, Ag, Sn, Cd, Se, In, Ga, and Ge are present in solid solution as opposed to the likely occurrence of Mo, Au, Tl, Sb, Pb, and Bi in microinclusions. Deleterious elements show low contents (Zn = 426-190 ppm, Se = 64-22 ppm, Sn = 53-1.3 ppm, Cd = 12-6.0 ppm, Tl < 11 ppm, Bi < 10 ppm, Ni < 2.5 ppm, As < 2.0 ppm, Hg < 3.8 ppm) relative to reference maximum contents before charge is incurred *sensu* Fontain (2013). The contents of Ag (136-23 ppm, up to 296 ppm) and Au (< 0.40 ppm) are also relatively low. In analyzed chalcopyrite grains, the contents of the potential *high-tech* by-products In (28-8.4 ppm, up to 49 ppm) and Ga (8.3-2.9 ppm, up to 24 ppm) are lower, and the contents of Ge (5.9-0.70 ppm, up to 80 ppm), higher, than in sphalerite from the respective deposits. General positive correlation trends between Zn, Cd, In, Ge, and Ga in chalcopyrite suggest varied coupled substitution mechanisms of Fe (+2 and +4) and Cu (+1 and +3) with fluctuating valences due to covalent bonding in this mineral.

A comprehensive sampling across the Sofía-D massive sulfide body in the María Teresa deposit revealed significant mineral and trace-element zonation. Mineral zones in Sofía-D include a core of dominant "barren" pyrite sheathed with facies of chalcopyrite (Cu zone) that grades outwards to sphalerite ± fahlore ± galena ± chalcopyrite (Zn zone) and galena + sphalerite ± fahlore ± barite (Pb – Zn – Ag zone) carapaces. Strong replacement of early sphalerite by chalcopyrite and metalliferous zonation strongly suggest zone refining. The contents of some trace elements in sphalerite and to a lesser extent in chalcopyrite display systematic vertical distribution patterns. In sphalerite, these include, bottom to top of the sulfide body, depletion in In, Cu, Mn, and Se and enrichment in Ge. This distribution agrees with the expected decrease of the crystallization temperature and/or volatile magmatic influx from the feeders of the massive mineralization. In chalcopyrite, the distributions of trace elements and Sc/Zn ratios are rather uneven except for constant enrichment in Bi (probably present as microinclusions) and Se towards the basal portion of the sulfide body. Unlike sphalerite, the trace element composition of chalcopyrite is strongly dependent on the co-crystallizing phases over physicochemical conditions. Co-crystallization and/or reequilibration of chalcopyrite with galena at shallower levels may therefore account for progressive depletion of Se in chalcopyrite.

The Sofía-D massive sulfide mineralization shows strong textural and mineralogical evidence of recrystallization during thermal metamorphism caused by nearby granodiorite intrusions. The impact of the thermal metamorphism in the absolute trace elements contents in sphalerite and chalcopyrite is unknown. However, the preservation of expected original trace element distribution patterns would suggest a closed metamorphic system and that element interdiffusion was local, probably attaining only contiguous sulfide grains. Accordingly, we propose that the distribution patterns described in this article for lattice-bound trace elements in sphalerite and chalcopyrite may be useful during exploration in order to trace the polarity of massive sulfide bodies in metamorphosed and tectonized terranes.

Acknowledgments

This study was economically supported by the Peruvian CONCYTEC-FONDECYT-World Bank project 107-2018-FONDECYT-BM-IADT-AV, the Spanish projects CGL2015–65824 and PID2019-105625RB-C21, and a Huiracocha Ph. D granted by the PUCP to D.B. Minera Colquisiri provided field and logistical support, access to the mine area, and the documents to prepare Fig. 2; its staff is most gratefully acknowledged, particularly Juan José Herrera, Edgar Pichardo, and Óscar Chirinos. We also thank Perilya-CORMIDOM for providing specimens from the Cerro de Maimón deposits. The analyzed material from Perubar and Palma was sampled (1998-2000) by Marc Polliand in the frame of his PhD thesis at the University of Geneva. The senior author acknowledges C.E. Nelson for insightful debate on the origin and classification of VMS deposits hosted in Cretaceous arc-related volcanic units in Cuba and the Dominican Republic. We appreciate the technical support by Xavier Llovet (CCiT-UB) during the acquisition of EPMA data, and by Peter Tollan (ETHZ) during the acquisition of LA-ICP-MS data. We are grateful to two anonymous reviewers for their constructive comments.

References

Aguirre, L., Levi, B., Nystrom, J. O., 1989. The link between metamorphism, volcanism and geotectonic setting during the evolution of the Andes. Geological Society Special Publications 43, 223-232.

Aillard, E., 1994. Kimmeridgian to Paleocene tectonic and geodynamic evolution of the Peruvian (and Ecuadorian) margin. In: Salfity, J.A. (Ed.), Cretaceous tectonics of the Andes. Vieweg, Wiesbaden, pp. 101-167.

Almodóvar, G.R., Yesares, L., Sáez, R., Toscano, M., González, F., Pons, J.M., 2019. Massive sulfide ores in the Iberian Pyrite Belt: Mineralogical and textural evolution. Minerals 9, 653.

Atherton, M.P., 1990. The Coastal Batholith of Peru: the product of rapid recycling of 'new' crust formed within rifted continental margin. Geological Journal 25, 337-349.

Atherton, M.P., Aguirre, L., 1992. Thermal and geotectonic setting of Cretaceous volcanic rocks near Ica, Peru, in relation to Andean crustal thinning. Journal of South American Earth Sciences 5, 47–69.

Atherton, M.P., Warden, V., Sanderson, L.M., 1985. The Mesozoic marginal basin of Central Peru: a geochemical study of within- plate-edge volcanism. In: Pitcher, W.S., Atherton, M.P., Cobbing, E.J., Beckinsale, R.D. (Eds.), Magmatism at a plate edge; the Peruvian Andes. Blackie, Glasgow, pp. 47–58.

Auclair, G., Fouquet, Y., Bohn, M., 1987. Distribution of selenium in high-temperature hydrothermal sulfide deposits at 13º North, East Pacific Rise. Canadian Mineralogist 25, 577-587.

Barton, P.B., Toulmin, P., 1966. Phase relations involving sphalerite in the Fe-Zn-S system. Economic Geology 61, 815-849

Bellisont, R., Boiron, M.C., Luais, B., Cathelineau, M., 2014. LA-ICP-MS analyses of minor and trace elements and bulk Ge isotopes in zoned Ge-rich sphalerites from the Noailhac – Saint-Salvy deposit (France): Insights into incorporation mechanisms and ore deposition processes. Geochimica et Cosmochimica Acta 126, 518-540.

Benavides-Cáceres, V., 1999. Orogenic evolution of the Peruvian Andes: The Andean Cycle. Society of Economic Geologists Special Publication 7, 61- 107.

Benites, D., Torró, L., Vallance, J., Laurent, O., Valverde, P.E., Kouzmanov, K., Chelle-Michou, C., Fontboté, L., 2021a. Distribution of indium, germanium, gallium and other minor and trace elements in polymetallic ores from a porphyry system: the Morococha District, Peru. Ore Geology Reviews 136, 104236.

Benites, D., Torró, L., Vallance, J., Laurent, O., Quispe. P., Rosas, S., Uzieda M.F., Holm-Denoma, C.S., Pianowski L.S., Camprubí, A., Colás, V., Fernández-Baca, A., Giraldo, L., Chelle-Michou, C., Sáez, J., Kouzmanov, K., Fontboté, L., 2021. Geology, mineralogy, and cassiterite geochronology of the Ayawilca Zn-Pb-Ag-In-Sn-Cu deposit, Pasco, Peru. Mineralium Deposita, accepted June 22, 2021.

Benzaazoua, M., Marion, P., Pinto, A., Migeon, H., Wagner, F.E., 2003. Tin and indium mineralogy within selected samples from the Neves Corvo ore deposit (Portugal): a multidisciplinary study. Minerals Engineering 16, 1291-1302.

Bueno Carreón, J.P., 2019. Herramientas de exploración aplicadas a la generación de nuevos targets en el yacimento VMS Cerro Lindo. Proexplo 2019, Lima, Extended Abstracts, pp. 332–340.

Bueno Carreón, J.P., Mendoza Mondragón, M., 2019. Caracterización litogeoquímica en el yacimiento VMS - Cerro Lindo y su relación con la mineralización para determinar vectores guías en exploración. Proexplo 2019, Lima, Extended Abstracts, pp. 196–201

Carvalho, J., Relvas, J., Pinto, A., Frenzel, M., Krause, J., Gutzmer, J., Gonçalves, M., 2018. Indium and selenium distribution in the Neves-Corvo deposit, Iberian Pyrite Belt, Portugal. Mineralogical Magazine 82, S5-S41.

Choquehuanca, S., 2020. Petrology, geochronology and geochemistry of the Lower Cretaceous in Palma volcanogenic massive sulfide (VMS) deposit, central Peru. Master Thesis, China University of Geosciences, Wuhan. 79 p.

Cobbing, E.J., 1999. The Coastal Batholith and other aspects of Andean magmatism in Peru, in: Castro, A., Fernández, C., Vigneresse, J.L. (Eds.), Understanding Granites: Integrating New and Classical Techniques. Geological Society London, Special Publications 168, pp. 111-122.

Cook, N.J., 1996. Mineralogy of the sulphide deposits at Sulitjelma, northern Norway. Ore Geology Reviews 11, 303-338.

Cook, N.J., Ciobanu, C.L., Pring, A., Skinner, W., Shimizu, M., Danyushevsky, L.V., Saini-Eidukat, B., Melcher, F., 2009. Trace and minor elements in sphalerite: a LA-ICPMS study. Geochimica et Cosmochimica Acta 73, 4761–4791.

Cook, N.J., Ciobanu, C.L., Williams, T., 2011. The mineralogy and mineral chemistry of indium in sulphide deposits and implications for mineral processing. Hydrometallurgy 108, 226-228.

Cook, N.J., Ciobanu, C.L., Brugger, J., Etschmann, B., Howard, D.L., de Jonge, M.D., Ryan, C., Paterson, D., 2012. Determination of the oxidation state of Cu in substituted Cu-In-Fe-bearing sphalerite via mu-XANES spectroscopy. American Mineralogist 97, 476–479.

Cook, N.J., Etschmann, B., Ciobanu, C.L., Geraki, K., Howard, D.L., Williams, T., Rae, N., Pring, A., Chen, G., Johannessen, B., Brugger, J., 2015. Distribution and substitution mechanism of Ge in a Ge-(Fe)-bearing sphalerite. Minerals 5, 117-132.

Cueva, E., Mamani, M., Rodríguez, R., 2019. Magmatismo y geoquímica del volcanismo Albiano Cenomaniano (Grupo Casma) y Maastrichtiano-Daniano entre Pucusana y Chimbote. XV Congreso Peruano de Geología, resúmenes extendidos. Sociedad Geológica de Perú, Peru, 9, pp. 921-924.

Donnay, G., Corliss, L.M., Donnay, J.D.H., Elliott, N., Hastings, J.M., 1958. Symmetry of magnetic structures: magnetic structure of chalcopyrite. Physical Review 112, 1917–1923.

Doyle, M.G., Allen, R.L., 2003. Subsea-floor replacement in volcanic-hosted massive sulfide deposits. Ore Geology Reviews 23, 183–222.

Dubé, B., Gosselin, P. Mercier-Langevin, P., Hannington, M., Galley, A., 2007. Gold-rich volcanogenic massive sulphide deposits, in: Goodfellow, W.D. (Ed.), Mineral Deposits of Canada: A Synthesis of Major Deposit-Types, District Metallogeny, the Evolution of Geological Provinces, and Exploration Methods: Geological Association of Canada, Mineral Deposits Division, Special Publication No. 5, pp. 75-94.

Eldridge, C.W., Barton, P.B., Ohmoto, H., 1983. Mineral textures and their bearing on formation of the Kuroko orebodies. Economic Geology Monograph, v. 5, pp. 241-281.

Farfán, C., Monge, R., Fontboté, L., 2019. Palma, yacimiento de Zn-Pb tipo VMS en una cuenca intra-arco del Cretácico Superior en Perú central, nuevos avances en exploración para un gran potencial. Proceedings of Proexplo 2019, Lima, Extended Abstracts pp. 209-215.

Fontboté, L., 2019. Volcanogenic Zn-Pb±Cu massive sulfide deposits in the Upper Cretaceous plutono-volcanic arc in central Peru. Proceedings of Proexplo 2019, Peru, Extended Abstracts, pp. 45-52.

Fountain, C., 2013. The whys and wherefores of penalty elements in copper concentrates, in: MetPlant: Metallurgical Plant Design and Operating Strategies, Australasian Institute of Mining and Metallurgy, Melbourne, Australia, v. 5, pp. 502–518

Franklin, J.M., Hannington, M.D., Jonasson, I.R., Barrie, C.T., 1998. Arc-related volcanogenic massive sulfide deposits, in: Metallogeny of volcanogenic arcs, British Columbia Geological Survey, Open-File 1998-8.

Franklin, J.M., Gibson, H.L., Jonasson, I.R., Galley, A.G., 2005. Volcanogenic Massive Sulfide Deposits. Economic Geology 100th Anniversary Volume, 523-560.

Frenzel, M.F., Hirsch, T., Gutzmer, J., 2016., Gallium, germanium, indium and other trace and minor elements in sphalerite as a function of the deposit type – A meta-analysis. Ore Geology Reviews 76, 52-78.

Frenzel, M., Bachmann, K., Carvalho, J.R.S., Relvas, J.M.R.S., Pacheco, N., Gutzmer, J., 2019. The geometallurgical assessment of by-products – geochemical proxies for the complex mineralogical deportment of indium at Neves-Corvo, Portugal. Mineralium Deposita 54, 959-982.

Galley, A.G., Hannington, M.D., Jonasson, I.R., 2007. Volcanogenic massive sulphide deposits. In: Goodfellow, W.D. (Ed.), Mineral Deposits of Canada: A Synthesis of Major Deposit-Types, District Metallogeny, the Evolution of Geological Provinces, and Exploration Methods. Geological Association of Canada, Mineral Deposits Division, Special Publication 5, pp. 141–161.

Gariepy, L., Hinostroza, J., 2013. El yacimiento tipo sulfuro masivo volcanogénico Cerro Lindo, Departamento de Ica, Perú. Proexplo, Lima, Extended Abstracts, 23 p.

Gemmell, J.B., Sharpe, R., Jonasson, I.A., Herzig, P.M., 2004. Sulfur Isotope Evidence for Magmatic Contributions to Submarine and Subaerial Gold Mineralization: Conical Seamount and the Ladolam Gold Deposit, Papua New Guinea. Economic Geology 99, 1711-1725.

George, L.L., Cook, N.J., Ciobanu, C.L., Wade, B.P., 2015. Trace and minor elements in galena: A reconnaissance LA-ICP-MS study. American Mineralogist 100, 548-569.

George, L.L., Cook, N.J., Crowe, B.B.P., Ciobanu, C.L., 2018. Trace elements in hydrothermal chalcopyrite. Mineralogical Magazine 82, 59-88.

Grant, H., Layton-Matthews, D., Peter, J.M., 2015. Distribution and controls on silver mineralization in the Hackett River Main Zone, Nunavut, Canada: An Ag- and Pb-enriched Archean volcanogenic massive sulfide deposit. Economic Geology 110, 943–982.

Gregory, D.D., Large, R.R., Halpin, J.A., Baturina, E.L., Lyons, T.W., Wu, S., Danyushevsky, L., Sack, P.J., Chappaz, A., Maslennikov, V.V., Bull, S.W., 2015. Trace element content of sedimentary pyrite in black shales. Economic Geology 110, 1389–1410.

Hall, S.R., Stewart, J.M., 1973. The crystal structure refinement of chalcopyrite, $CuFeS_2$. Acta Crystallographica Section B: Structural Crystallography and Crystal Chemistry 29, 579–585.

Hannington, M.D., Scott, S.D., 1989. Sulfidation equilibria as guides to gold mineralization in volcanogenic sulfides: evidence from sulfide mineralogy and the composition of sphalerite. Economic Geology 84, 1978–1995.

Hannington, M.D., Jonasson, I.R., Herzig, P.M., Petersen, S., 1995. Physical and chemical processes of seafloor mineralization, in: Humphris, S.E., Zierenberg, R.A., Mullineaux, L.S., Thomson, R.E. (Eds.), Seafloor hydrothermal systems—Physical, chemical, biological, and geological interactions. American Geophysical Union Geophysical Monograph 91, pp. 115–157.

Hannington, M.D., Galley, A.G., Herzig, P.M., Petersen, S., 1998. Comparison of the TAG mound and stock- work complex with Cyprus-type massive sulfide deposits, in: Herzig, P.M., Humphris, S.E., Miller, D.J., Zierenberg, R.A. (Eds.), TAG—Drilling an active hydrothermal system on a sediment-free slow-spreading ridge, site 957: Proceedings of the Ocean Drilling Program, Scientific Results 158, p. 389–415.

Herrington, R., Maslennikov, V., Zaykov, V., Seravkin, I., Kosarev, A., Buschmann, B., Orgeval, J.J., Holland, N., Tesalina, S., Nimis, P., Armstrong, R., 2005. 6: classification of VMS deposits: lessons from the uralides. Ore Geology Reviews 27, 203–237.

Hildebrand, R.S., Whalen, J.B., 2014. Arc and Slab-Failure Magmatism in Cordilleran Batholiths I – The Cretaceous Coastal Batholith of Peru and its Role in South American Orogenesis and Hemispheric Subduction Flip. Geoscience Canada 41, 255-282.

Hollis, S.P., Roberts, S., Earls, G., Herrington, R., Cooper, M.R., Piercey, S.J., Archibald, S.M., Moloney, M., 2014. Petrochemistry and hydrothermal alteration within the Tyrone igneous complex, Northern Ireland: implications for VMS mineralization in the British and Irish Caledonides. Mineralium Deposita 49, 575–593.

Huston, D.L., Sie, S.H., Suter, G.F., Cooke, D.R., Both, R.A., 1995. Trace elements in sulfide minerals from eastern Australian volcanic-hosted massive sulfide deposits; Part I, Proton microprobe analyses of pyrite, chalcopyrite, and sphalerite, and Part II, Selenium levels in pyrite; comparison with delta 34 S values and implications for the source of sulfur in volcanogenic hydrothermal systems. Economic Geology 90, 1167–1196.

INGEMMET, 2000. Mapa geológico digitalizadp del Perú (Escala 1:1,000,000). Instituto Geológico, Minero y Metalúrgico, Lima. CD-ROM.

Keith, M., Haase, K.M., Schwarz-Schampera, U., Klemd, R., Petersen, S., Bach, W., 2014. Effect of temperature, sulfur and oxygen fugacity on the composition of sphalerite from submarine hydrothermal vents. Geology 42, 699–702.

Koski, R.A., Mosier, D.L., 2012. Deposit type and associated commodities in volcanogenic massive sulfide occurrence model. U.S. Geological Survey Scientific Investigations Report 2010–5070 –C, chapter 2, 8 p.

Layton-Matthews, D., Peter, J.M., Scott, S.D., Leybourne, M.I., 2008. Distribution, Mineralogy, and Geochemistry of Selenium in Felsic Volcanic-Hosted Massive Sulfide Deposits of the Finlayson Lake District, Yukon Territory, Canada. Economic Geology 103, 61–88.

Li, Y., Kawashima, N., Li, J., Chandra, A.P., Gerson, A.R., 2013. A review of the structure, and fundamental mechanisms and kinetics of the leaching of chalcopyrite. Advances in Colloid and Interface Science,197, 1–32.

Lockington, J.A., Cook, N.J., Ciobanu, C.L., 2014. Trace and minor elements in sphalerite from metamorphosed sulfide deposits. Mineralogy and Petrology 108, 873-890.

Martín, M., Draper, G., 1999. Mapa geológico de la hoja 6172-I (Hatillo) a escala 1:50 000 (SYSMIN, Proyecto C). Consorcio ITGE-PROINTEC-INYPSA. Dirección General de Minería, Santo Domingo.

Martin, A.J., Keith, M., McDonald, I., Haase, K.M., McFall, K.A., Klemd, R., MacLeod, C.J., 2019. Trace element systematics and ore-forming processes in mafic VMS deposits: Evidence from the Troodos ophiolite, Cyprus. Ore Geology Reviews 106, 205-225.

Mégard, F., 1984. The Andean orogenic period and its major structures in central and northern Peru. Journal of the Geological Society 141, 893–900.

Monecke, T., Petersen, S., Hannington, M.D., 2014. Constraints on Water Depth of Massive Sulfide Formation: Evidence from Modern Seafloor Hydrothermal Systems in Arc-Related Settings. Economic Geology 109, 2079-2101.

Murakami, H., Ishihara, S., 2013. Trace elements of indium-bearing sphalerite from tin-polymetallic deposits in Bolivia, China and Japan: A femto-second LA-ICPMS study. Ore Geology Reviews 53, 223–243.

Nelson, C.E., Proenza, J.A., Lewis, J.F., López-Kramer, J., 2011. The metallogenic evolution of the Greater Antilles. Geologica Acta 9, 229–264.

Nimis, P., Omenetto, P., Tesalina, S.G., Zaykov, V.V., Tartarotti, P., Orgéval, J.-J., 2003. Peculiarities of some mafic–ultramafic-hosted massive sulfide deposits from southern Urals – A likely forearc occurrence, in: Eliopoulos, D.G., et al., (Eds.), Mineral Exploration and Sustainable Development. Millpress, Rotterdam, pp. 627–630.

Ohmoto, H., 1996. Formation of volcanogenic massive sulfide deposits: The Kuroko perspective. Ore Geology Reviews 10, 135-177.

Perilya, 2020. Cerro de Maimón [accessed July 5, 2021]

Peter, J.M., Leybourne, M.I., Scott, S.D., Gorton, M.P., 2014. Geochemical constraints on the tectonic setting of basaltic host rocks to the Windy Craggy Cu-Co-Au massive sulphide deposit, northwestern British Columbia. International Geology Review 56, 1484-1503.

Petersen, S., Monecke, T., Westhues, A., Hannington, M.D., Gemmell, J.B., Sharpe, R., Peters, M., Strauss, H., Lackschewitz, K., Augustin, N., Gibson, H., Kleeberg, R., 2014. Drilling shallow-water massive sulfides at the Palinuro volcanic complex, Aeolian island arc, Italy. Economic Geology 109, 2129–2158.

Pichardo, E., Fontboté, L., Mena, T., Chirinos, O., Halter, W., 2019. El yacimiento de Zn-Pb-Cu-Ag tipo VMS María Teresa, Perú: Geología y exploración. Proceedings of Proexplo 2019, Peru, Extended Abstracts, pp. 209-215.

Piercey, S.J., 2011. The setting, style, and role of magmatism in the formation of volcanogenic massive sulfide deposits. Mineralium Deposita 46, 449–471.

Pitcher, W.S., 1985. A multiple and composite batholith, in: Pitcher, W.S, Atherton, M.P., Cobbing, E.J., Beckinsale, R.D. (Eds.), Magmatism at a plate edge: The Peruvian Andes. Blackie, Glasgow, pp. 93-101.

Polliand, M., 2006. Genesis, evolution, and tectonic setting of the Upper Cretaceous Perubar Ba-Pb-Zn volcanic-hosted massive sulfide deposit, Central Peru.Terre & Environnement 60, 141 p.

Polliand, M., Fontboté, L., Spangenberg, J., 1999. Tracing back sulfur isotope reequilibration due to contact metamorphism: A case study from the Perubar VMS deposit, Central Peru. In: Stanley, C.J. et al. (Eds.), Mineral deposits: processes to processing, 5th biennial SGA meeting, London. Balkema, Rotterdam, pp. 967- 970.

Polliand, M., Schaltegger, U., Frank, M., Fontboté, L., 2005. Formation of intra-arc volcano-sedimentary basins in the western flank of the central Peruvian Andes during Late Cretaceous oblique subduction—field evidence and constraints from U-Pb ages and Hf isotopes. International Journal of Earth Sciences 94, 231–242.

Revan, M.K., Genç, Y., Maslennikov, V.V., Maslennikova, S.P., Large, R.R., Danyushevsky, L.V., 2014. Mineralogy and trace-element geochemistry of sulfide minerals in hydrothermal chimneys from the Upper-Cretaceous VMS deposits of the eastern Pontide orogenic belt (NE Turkey). Ore Geology Reviews 63, 129-149.

Ridley, W.I, 2012. Geochemical characteristics in volcanogenic massive sulfide occurrence model. U.S. Geological Survey Scientific Investigations Report 2010–5070 –C, chap. 14, 18 p.

Romero, D., Quispe, J., Carlotto, V., Tassinari, C., 2008. Los depósitos de la cuenca Maastrichtiano - Daniano: relación con los yacimientos tipo sulfuros masivos volcanogénicos de Pb - Zn - Cu; Perú central. Proceedings of the Congreso Peruano de Geología, 14, Lima (CD – ROM). Sociedad Geológica del Perú, Lima, 6 p.

Scherrenberg, A.F., Jacay, J., Holcombe, R.J., Rosenbaum, G., 2012. Stratigraphic variations across the Marañón Fold-Thrust Belt, Peru: Implications for the basin architecture of the West Peruvian Trough. Journal of South American Earth Sciences 38, 147-158.

Schmidt, M.A., Leybourne, M.I., Peter, J.M., Petts, D., Layton-Matthews, D., 2019. Fluid inclusion LA-ICP-MS and whole rock geochemical investigation of possible magmatic contributions to the giant Windy Craggy Besshi-type VMS deposit, in: Rogers, N. (Ed.), Targeted Geoscience Initiative: 2018 report of activities, Geological Survey of Canada, Open File 8549, pp. 189–204. https://doi.org/10.4095/313651.

Shanks III, W.C.P., Thurston, R., 2012. Volcanogenic massive sulfide occurrence model: U.S. Geological Survey Scientific Investigations Report 2010–5070–C, 345 pp.

Sillitoe, R.H., Hannington, M.D., Thompson, J.F.H., 1996. High sulfidation deposits in the volcanogenic massive sulfide environment. Economic Geology 91, 204-212.

Soler, P., 1991. El volcanismo Casma del Perú Central: cuenca marginal abortada o simple arco volcanico?. VII Congreso Peruano de Geología, Lima, Volumen de Resúmenes Extendidos, Sociedad Geológica de Perú, pp. 659–663.

Steinmüller, K., Chacón Abad, N., Grant, B., 2000. Volcanogenic massive sulfides in Peru. In: Sherlock, R.L., Logan, M.A.V. (Eds.), VMS Deposits of Latin America. Geological Association of Canada, Mineral Deposits Division 2, pp. 423–437.

Tegart, P., Allen, G., Carstensen, A., 2000, Regional setting, stratigraphy, alteration and mineralization of the Tambo Grande VMS district, Piura department, northern Peru. In: Sherlock, R.L., Logan, M.A.V. (Eds.), VMS Deposits of Latin America. Geological Association of Canada, Mineral Deposits Division 2, pp. 375–405.

Tivey, M.K., 2007. Generation of seafloor hydrothermal vent fluids and associated mineral deposits. Oceanography 20, 50-65.

Tornos, F., Peter, J.M., Allen, R., Conde, C., 2015. Controls on the sitting and style of volcanogenic massive sulphide deposits. Ore Geology Reviews 68, 142-163.

Torró, L., Proenza, J.A., Melgarejo, J.C., Alfonso, P., Farré de Pablo, J., Colomer, J.M., García- Casco, A., Gubern, A., Gallardo, E., Cazañas, X., Chávez, C., del Carpio, R., León, P., Nelson, C., Lewis, J.F., 2016a. Mineralogy, geochemistry and sulfur isotope characterization of the Cerro de Maimón (Dominican Republic), San Fernando and Antonio (Cuba): Lower Cretaceous VMS deposits associated to the subduction initiation of the Proto-Caribbean lithosphere within a fore-arc. Ore Geology Reviews 72, 794–817.

Torró, L., Garcia-Casco, A., Proenza, J.A., Blanco-Quintero, I.F., Gutiérrez-Alonso, G., Lewis, J.F., 2016b. High-pressure greenschist to blueschist facies transition in the Maimón Formation (Dominican Republic) suggests mid-Cretaceous subduction of the Early Cretaceous Caribbean Arc. Lithos 266–267, 309–331.

Torró, L., Proenza, J.A., Marchesi, C., García-Casco, A., Lewis, J.F., 2017. Petrogenesis of meta-volcanic rocks from the Maimón Formation (Dominican Republic): Geochemical record of the nascent Greater Antilles paleo-arc. Lithos 278–281, 255–273.

Torró, L., Proenza, J.A., Espaillat, J., Belén-Manzueta, A.J., Román-Alday, M.C., Amarante, A., González, N., Espinoza, J., Román-Alpiste, M.J., Nelson, C.E., 2018a. The Discovery of the Romero VMS Deposit and Its Bearing on the Metallogenic Evolution of Hispaniola during the Cretaceous. Minerals 8, 507, 24 p.

Torró, L., Proenza, J.A., Rojas-Agramonte, Y., Garcia-Casco, A., Yang, J.-H., Yang, Y.-H., 2018b. Recycling in the subduction Factory: Archaean to Permian zircons in the oceanic Cretaceous Caribbean island-arc (Hispaniola). Gondwana Research 54, 23–37.

Trofimov, N.D., Trigub, A.L., Tagirov, B.R., Filimonova, O.N., Evstigneeva, P.V., Chareev, D.A., Kvashnina, K.O., Nickolsky, M.S., 2020. The State of Trace Elements (In, Cu, Ag) in Sphalerite Studied by X-Ray Absorption Spectroscopy of Synthetic Minerals. Minerals 10, 640.

Vela, C., 1997. Nueva concepción estratigráfica de la subcuenca de Lima. IX Congreso Peruano de Geología, Resúmenes Extendidos, Sociedad Geológica de Perú, Peru, pp. 409–412.

Vidal, C.C.E., 1987. Kuroko-type deposits in the Middle-Cretaceous marginal basin of central Peru. Economic Geology 82, 1409–1430.

Votorantim., 2017. Cerro Lindo polymetallic mine, NI 43-101 Technical Report on Operations, 315 p.

Winter, L.S., Tosdal, R.M., Franklin, J.M., Tegart, P., 2004. A Reconstructed Cretaceous Depositional Setting for Giant Volcanogenic Massive Sulfide Deposits at Tambogrande, Northwestern Peru. Society of Economic Geologists Special Publication 11, 319–340.

Winter, L.S., Tosdal, R.M., Mortensen, J.K., Franklin, J.M., 2010. Volcanic stratigraphy and geochronology of the Cretaceous Lancones Basin, northwestern Peru: position and timing of giant VMS deposits. Economic Geology 105, 713–742.

Ye, L., Cook, N.J., Ciobanu, C.L., Yuping, L., Qian, Z., Tiegeng, L., Wei, G., Yulong, Y., Danyushevskiy, L., 2011. Trace and minor elements in sphalerite from base metal deposits in South China: A LA-ICP-MS study. Ore Geology Reviews 39, 188-217.

Yeats, C.J., Parr, J.M., Binns, R.A., Gemmell, J.B., Scott, S.D., 2014. The SuSu Knolls Hydrothermal Field, Eastern Manus Basin, Papua New Guinea: An Active Submarine High-Sulfidation Copper-Gold System. Economic Geology 109, 2207-2226.

Zaccarini, F., Garuti, G., 2008. Mineralogy and chemical composition of VMS deposits of northern Apennine ophiolites, Italy: evidence for the influence of country rock type on ore composition. Mineralogy and Petrology 94, 61-83.

Figure captions

Fig. 1. Geologic map of the Peruvian Coastal Batholith and Mesozoic Western Peruvian Trough (WPT) with related volcano-sedimentary basins hosting massive sulfide deposits. Modified from Polliand et al. (2005). Distribution of the Cretaceous Peruvian Costal Batholith and strata after the digital version of the geological map of Peru (INGEMMET, 2000).

Fig. 2. Representative schematic cross-section across the Sofía D massive sulfide body in the María Teresa VMS deposit, Peru (redrawn from geological documents of the María Teresa Mine geological department as of December 2020).

Fig. 3. (A) Geographic location of the Early Cretaceous boninite and island arc tholeiite volcanic series and ophiolitic peridotites along the Greater Antilles. (B) Geological map of the Maimón Formation and surrounding Early Cretaceous arc-related volcanic units (modified from Martín and Draper, 1999).

Fig. 4. Drill core photographs of sulfide mineralization from the Sofía-D massive sulfide body in the María Teresa VMS deposit. (A-C) Semi-massive sulfide ore dominated by medium-grained pale-brown sphalerite grains partially replaced by an assemblage of pyrite and chalcopyrite. (D) Massive sulfide ore composed of coarse-grained red-brownish sphalerite grains cut by irregular veinlets of chalcopyrite and pyrite. (E) Dark red, medium-sized sphalerite partially replaced by an assemblage of pyrite and chalcopyrite and the whole assemblage cut by thin, irregular chalcopyrite veinlets. (F) Coarse-grained pyrrhotite and chalcopyrite in a sample picked up close to a contact with a porphyritic andesitic dyke. (G) Silicified volcaniclastic rock with chalcopyrite mineralization along clast contacts. (F) Irregular veinlets of chalcopyrite in a silicified intrusive rock. Key: cpy = chalcopyrite; po = pyrrhotite; py = pyrite; qz = quartz; sl = sphalerite.

Fig. 5. Photomicrographs (reflected light) of textural features in the samples from the Sofía-D massive sulfide bodies in the María Teresa deposit used for this study. (A) Foam textured pyrite with triple junctions at 120º along with interstitial chalcopyrite and sphalerite. (B) Anhedral roundish and sub-roundish pyrite grains with irregular fractures are surrounded by an assemblage of sphalerite, galena and tennantite. (C-D) Anhedral, sub-roundish pyrite and subhedral arsenopyrite grains both with internal fractures with interstitial chalcopyrite, sphalerite, and tennantite. (E) Detail of a sphalerite-galena-tennantite intergrowth between roundish pyrite grains; note the general foam texture described by the contacts between all phases. (F) Pervasive replacement of sphalerite by chalcopyrite along borders and as fines disseminations (chalcopyrite disease texture). (G) Detail of chalcopyrite with exsolutions of sharply bounded cubanite laths. (H) Detail of minute inclusions of auriferous silver in chalcopyrite veinlets crosscutting arsenopyrite.

Key: apy = arsenopyrite; Ag_Au = auriferous silver; cbn = cubanite; cpy = chalcopyrite; mag = magnetite; po = pyrrhotite; py = pyrite; qz = quartz; sl = sphalerite; tn = tennantite.

Fig. 6. Paragenetic sequence for the Sofía-D sulfide body in the Calera area, María Teresa VMS deposit. Thick bars indicate higher abundances and dashed lines, lesser abundances.

Fig. 7. Boxplots of log-transformed element contents (A-I) and crystallization temperature (J) according to the GGIMFis geothermometer of Frenzel et al. (2016) for sphalerite at different depths along the drill core 34-18-S in the mine section 300 across the Sofía-D massive sulfide body, María Teresa deposit (LA-ICP-MS data). Box-and-whisker plots provide IQR (box), 1.5 IQR (whiskers), median (line), and outliers (circles).

Fig. 8. Boxplots of log-transformed element contents in chalcopyrite at different depths along the drill core 34-18-S in the mine section 300 across the Sofía-D massive sulfide body, Calera sector, María Teresa deposit (LA-ICP-MS data). Box-and-whisker plots provide IQR (box), 1.5 IQR (whiskers), median (line), and outliers (circles).

Fig. 9. Binary plots showing inter-element correlations in sphalerite: (A) Fe vs. Zn, (B) Ag vs. Pb, (C) Ag vs. Sb, and (D) Sb+Sn vs. Ag+Pb. Dashed lines represent 1:1 molar correlation. Additionally, contents are presented in box-and-whisker plots, which provide IQR (box), 1.5 IQR (whiskers), median (line) and outliers (circles). The composition of sphalerite from other VMS deposits worldwide are shown for comparison (data from Carvalho et al., 2018, Cook et al., 2019, Revan et al., 2014, and Ye et al., 2011).

Fig. 10. Binary plots showing inter-element correlations in sphalerite: (A) In vs. Cu, (B) Ga vs. Cu, and (C) Sn+In+Ge+Ga vs. Cu+Ag. Dashed lines represent 1:1 molar correlation. Additionally, contents are presented in box-and-whisker plots, which provide IQR (box), 1.5 IQR (whiskers), median (line) and outliers (circles). The composition of sphalerite from other VMS deposits worldwide are shown for comparison (data from Carvalho et al., 2018, Cook et al., 2019, Revan et al., 2014, and Ye et al., 2011).

Fig. 11. Binary plots showing inter-element correlations in chalcopyrite: (A) Bi vs. Cu, (B) In vs. Cu, (C) Ga vs. Cu, and (D) Sn+In+Ge+Ga vs. Cu+Ag. Dashed lines represent 1:1molar correlation. Additionally, contents are presented in box-and-whisker plots, which

provide IQR (box), 1.5 IQR (whiskers), median (line) and outliers (circles). The composition of sphalerite from other VMS deposits worldwide are shown for comparison (data from Carvalho et al., 2018, George et al., 2018, and Revan et al., 2014).

Table captions

Table 1. Summary of element contents in sphalerite from the María Teresa, Perubar, Palma, and Cerro de Maimón VMS deposits (LA-ICP-MS data).

Table 2. Summary of element contents in chalcopyrite from the María Teresa and Cerro de Maimón VMS deposits (LA-ICP-MS data).

Table 3. Summary of LA-ICP-MS data for sphalerite from subduction-related VMS deposits reported in the literature.

Table 4. Summary of LA-ICP-MS data for chalcopyrite from subduction-related VMS deposits reported in the literature.

Supplementary material

Table S1. List of samples and their location.

Table S2. Representative EPMA analyses of sphalerite and chalcopyrite from the María Teresa, Palma and Perubar VMS deposits in Peru. Structural formula of sphalerite was normalized to S = 1. Structural formula of chalcopyrite was normalized to S = 2.

Table S3. LA-ICP-MS trace element analyses on sulfides and reference materials.

Fig. S1. Photomicrographs (reflected light) of textural features in samples used for this study from the Perubar deposit. **A)** Pyrrhotite intergrown with massive sphalerite. A minute (4 µm) grain of electrum occurs in the contact between both minerals. **B)** Sphalerite-galena assemblage with local chalcopyrite inclusions in a matrix of baryte. **C)** Pyrrhotite, pyrite, sphalerite, and chalcopyrite. A pyrite crystal shows microporosity in its core and massive overgrowth bands. **D)** Subhedral magnetite crystal surrounded by massive sphalerite, the latter also including pyrite and pyrrhotite inclusions. **E)** Elongated molybdenite crystal in contact with sphalerite. **F)** Electrum grains (4-8 µm) along pyrite grain boundaries. Pyrrhotite partly replaced by pyrite and marcasite. Abbreviations: bar: **baryte**; **cpy**: chalcopyrite; **el**: electrum; **gn**: galena; **mc**: marcasite; **mt**: magnetite; **mb**: molybdenite; **py**: pyrite; **po**: pyrrhotite; **sl**: sphalerite.

Fig. S2. Photomicrographs (reflected light) of textural features in samples used for this study from the Palma deposit. **A)** Aggregates of spheroidal and subhedral pyrite grains cemented by sphalerite and galena. **B)** Mass of sphalerite and minor galena along with relictic pyrrhotite. **C)** Sphalerite replacement of pyrrhotite; sphalerite also lines voids in cariated pyrite. **D)** Pyrite partly showing "atoll-like texture" in massive sphalerite. **E)** Pyrrhotite aggregates replaced by massive sphalerite and galena. **F)** Subhedral pyrite in massive sphalerite with pyrrhotite relicts. Fine disseminations of chalcopyrite in sphalerite. Abbreviations: **cpy**: chalcopyrite; **gn**: galena; **py**: pyrite; **po**: pyrrhotite; **sl**: sphalerite.

Fig. S3. Representative downhole LA-ICP-MS spectra for selected elements in sphalerite (A-D) and chalcopyrite (E-F).

Figure 1

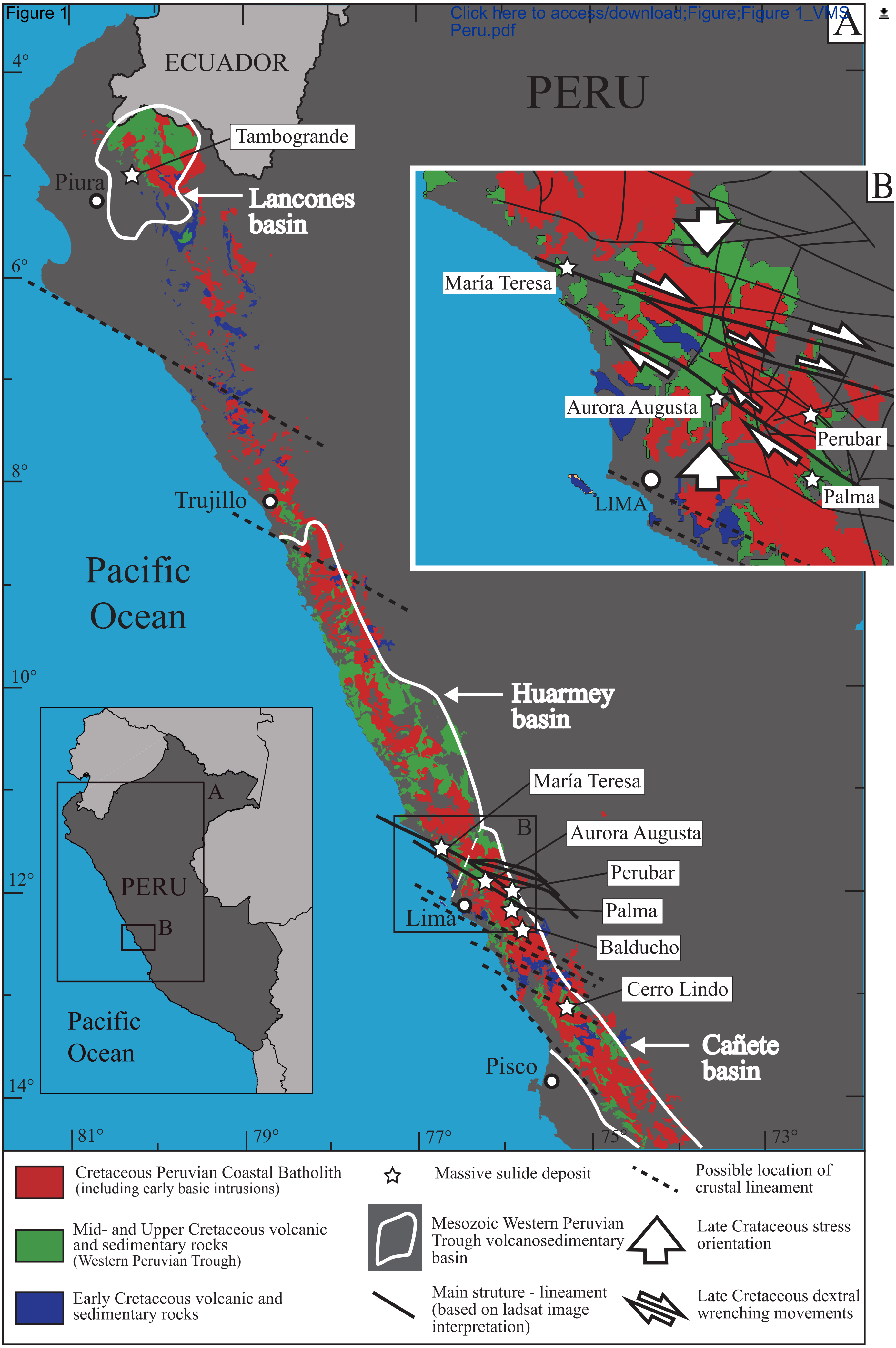
A
ECUADOR
PERU
4°
6°
8°
10°
12°
14°
Tambogrande
Piura
Lancones basin
Trujillo
Pacific Ocean
Huarmey basin
María Teresa
Aurora Augusta
Perubar
Palma
Balducho
Cerro Lindo
Lima
Pisco
Cañete basin
B
81°
79°
77°
75°
73°
PERU
Pacific Ocean
A
B
María Teresa
Aurora Augusta
Perubar
Palma
LIMA
Cretaceous Peruvian Coastal Batholith (including early basic intrusions)
Mid- and Upper Cretaceous volcanic and sedimentary rocks (Western Peruvian Trough)
Early Cretaceous volcanic and sedimentary rocks
Massive sulide deposit
Mesozoic Western Peruvian Trough volcanosedimentary basin
Main struture - lineament (based on ladsat image interpretation)
Possible location of crustal lineament
Late Crataceous stress orientation
Late Cretaceous dextral wrenching movements

Figure 2

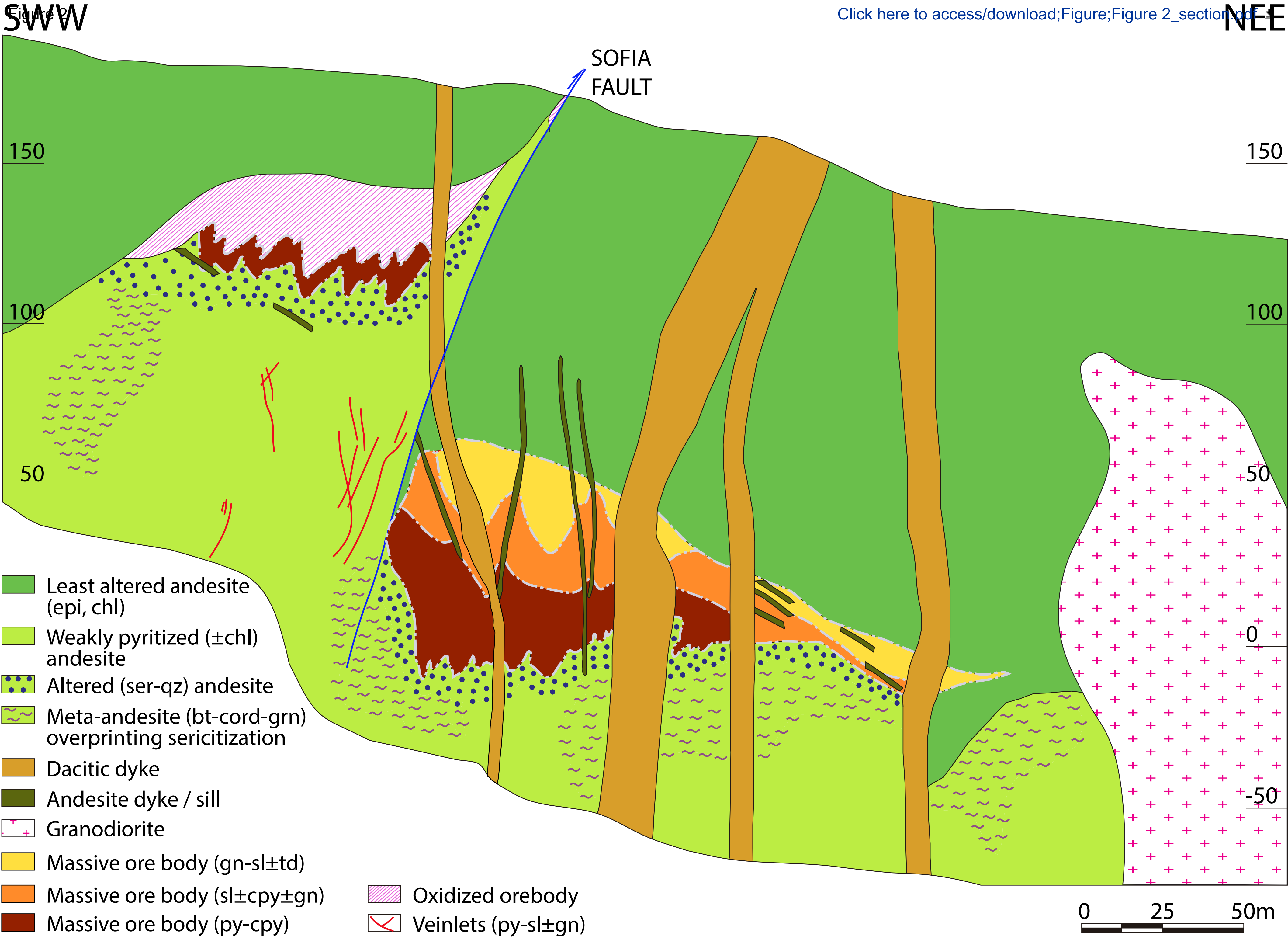
SWW
NEE
SOFIA FAULT
150
100
50
150
100
50
0
-50
Least altered andesite (epi, chl)
Weakly pyritized (±chl) andesite
Altered (ser-qz) andesite
Meta-andesite (bt-cord-grn) overprinting sericitization
Dacitic dyke
Andesite dyke / sill
Granodiorite
Massive ore body (gn-sl±td)
Massive ore body (sl±cpy±gn)
Massive ore body (py-cpy)
Oxidized orebody
Veinlets (py-sl±gn)
0
25
50m

Figure 3

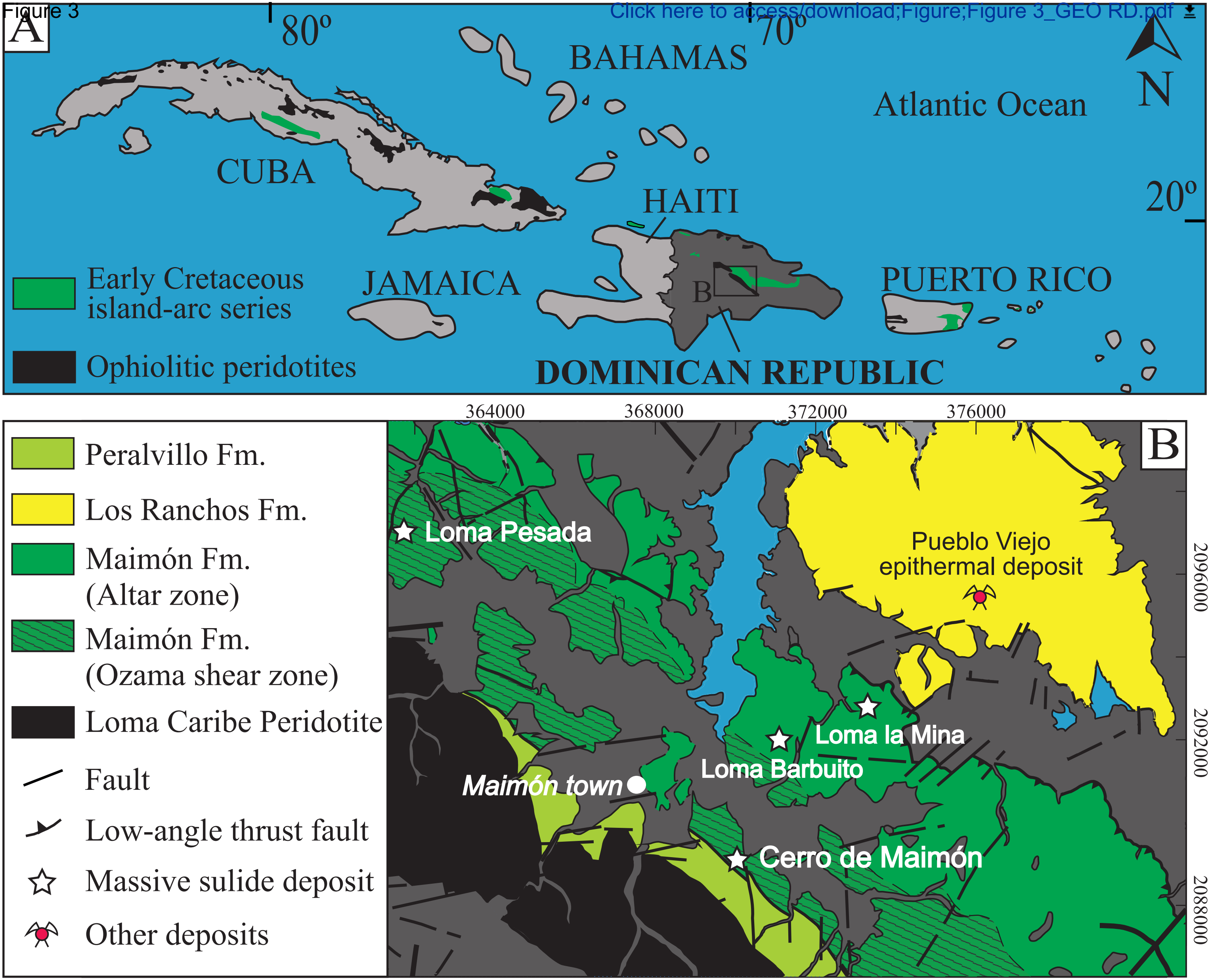
A
80º
70º
BAHAMAS
Atlantic Ocean
N
CUBA
20º
HAITI
JAMAICA
B
PUERTO RICO
DOMINICAN REPUBLIC
Early Cretaceous island-arc series
Ophiolitic peridotites
364000
368000
372000
376000
B
2096000
2092000
2088000
Peralvillo Fm.
Los Ranchos Fm.
Maimón Fm. (Altar zone)
Maimón Fm. (Ozama shear zone)
Loma Caribe Peridotite
Fault
Low-angle thrust fault
Massive sulide deposit
Other deposits
Loma Pesada
Pueblo Viejo epithermal deposit
Loma la Mina
Loma Barbuito
Maimón town
Cerro de Maimón

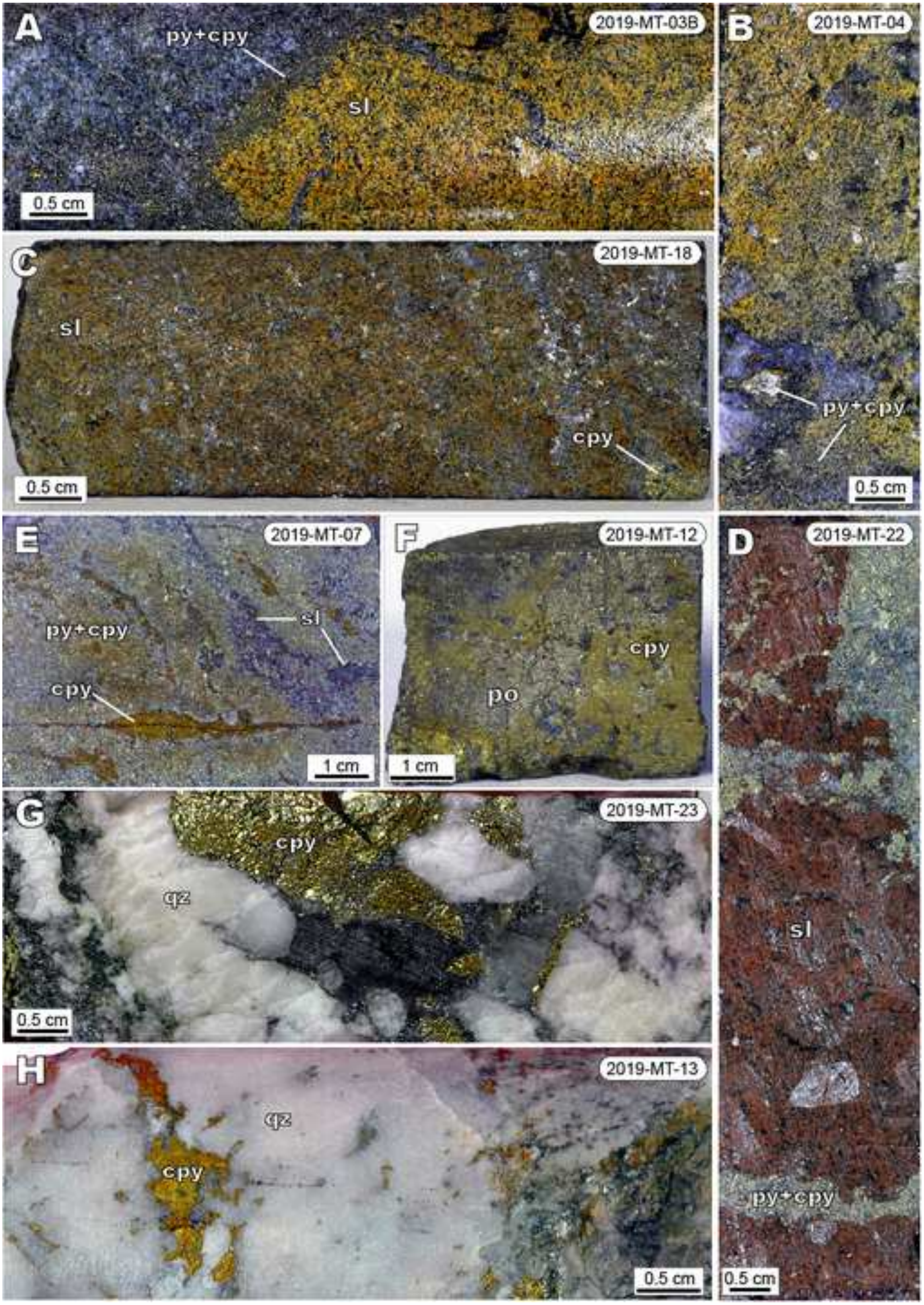
A
2019-MT-03B
py+cpy
sl
0.5 cm
B
2019-MT-04
py+cpy
0.5 cm
C
2019-MT-18
sl
cpy
0.5 cm
E
2019-MT-07
py+cpy
sl
cpy
1 cm
F
2019-MT-12
cpy
po
1 cm
D
2019-MT-22
sl
py+cpy
0.5 cm
G
2019-MT-23
cpy
qz
0.5 cm
H
2019-MT-13
qz
cpy
0.5 cm

Figure 5

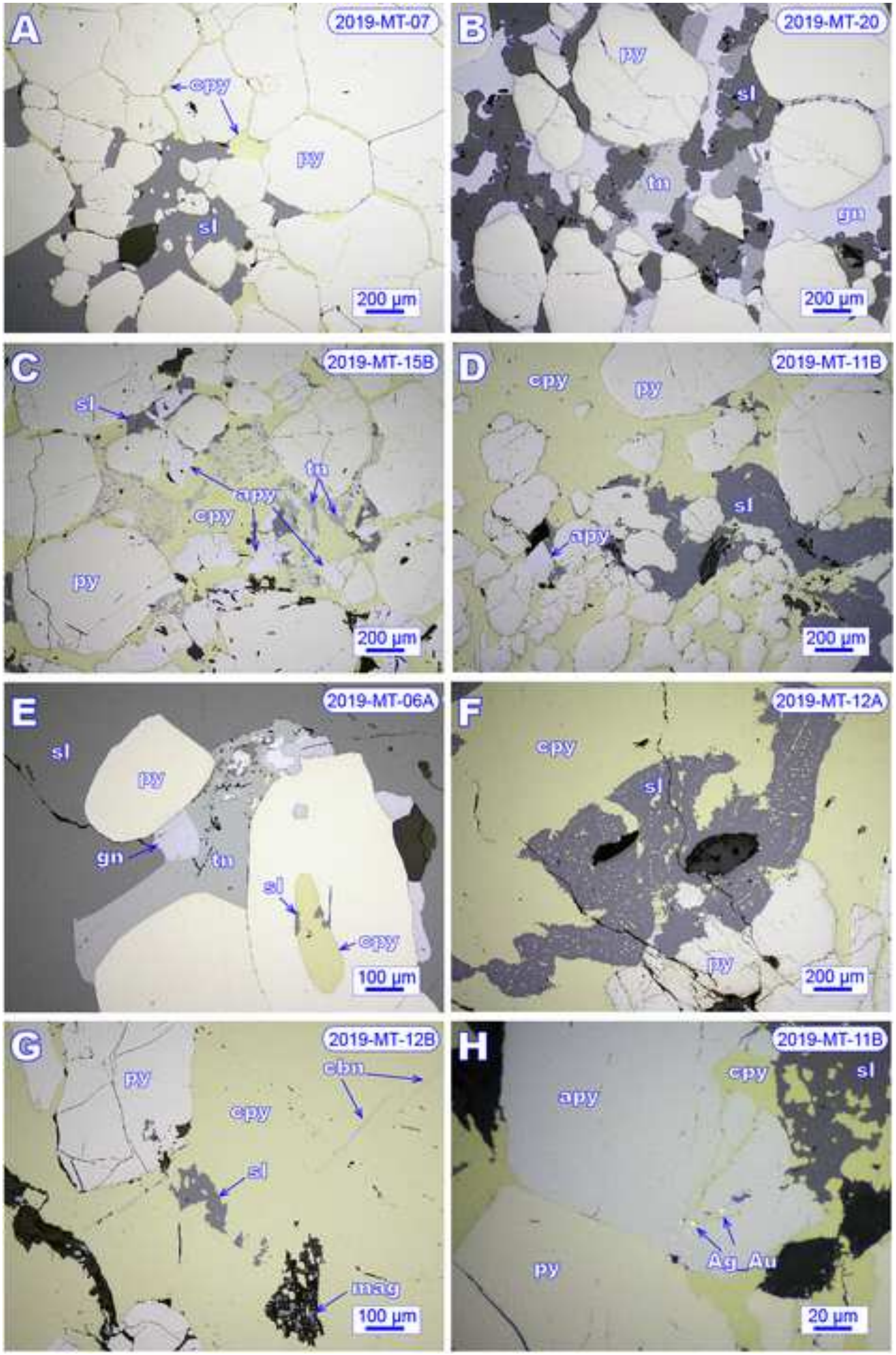
A
2019-MT-07
cpy
py
sl
200 µm
B
2019-MT-20
py
sl
tn
gn
200 µm
C
2019-MT-15B
sl
tn
apy
cpy
py
200 µm
D
2019-MT-11B
cpy
py
sl
apy
200 µm
E
2019-MT-06A
sl
py
gn
tn
sl
cpy
100 µm
F
2019-MT-12A
cpy
sl
py
200 µm
G
2019-MT-12B
py
cbn
cpy
sl
mag
100 µm
H
2019-MT-11B
apy
cpy
sl
py
Ag
Au
20 µm

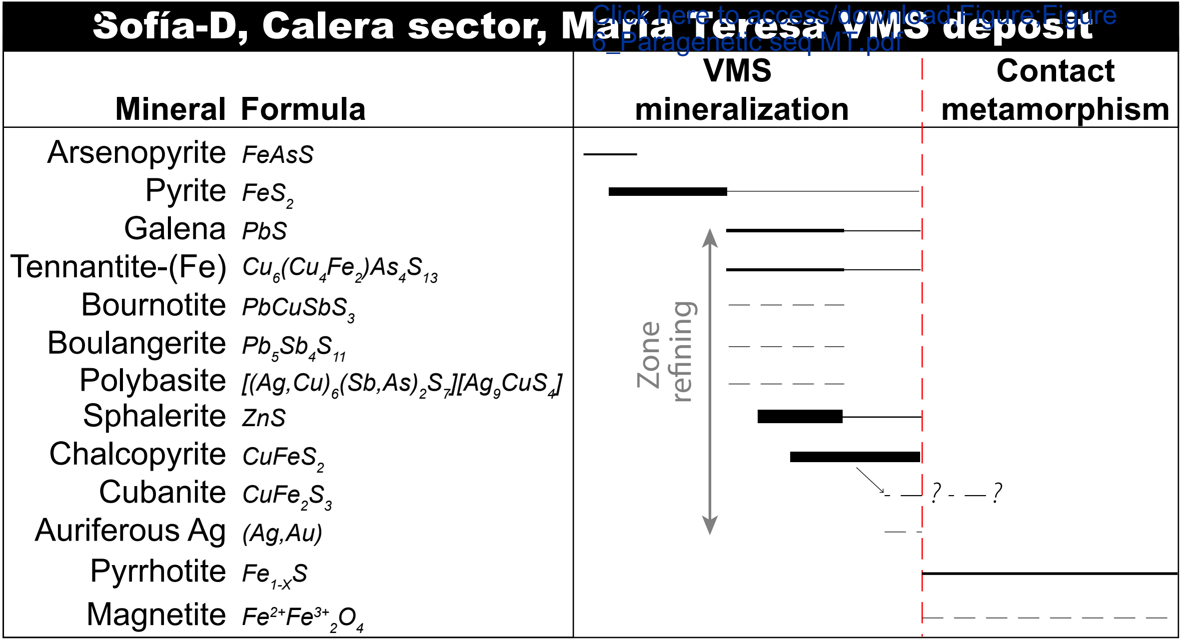
Sofía-D, Calera sector, María Teresa VMS deposit
Mineral
Formula
VMS mineralization
Contact metamorphism
Arsenopyrite $FeAsS$
Pyrite FeS_2
Galena PbS
Tennantite-(Fe) $Cu_6(Cu_4Fe_2)As_4S_{13}$
Bournotite $PbCuSbS_3$
Boulangerite $Pb_5Sb_4S_{11}$
Polybasite $[(Ag,Cu)_6(Sb,As)_2S_7][Ag_9CuS_4]$
Sphalerite ZnS
Chalcopyrite $CuFeS_2$
Cubanite $CuFe_2S_3$
Auriferous Ag (Ag,Au)
Pyrrhotite $Fe_{1-X}S$
Magnetite $Fe^{2+}Fe^{3+}{}_2O_4$
Zone refining
?
?

Figure 7

Sphalerite

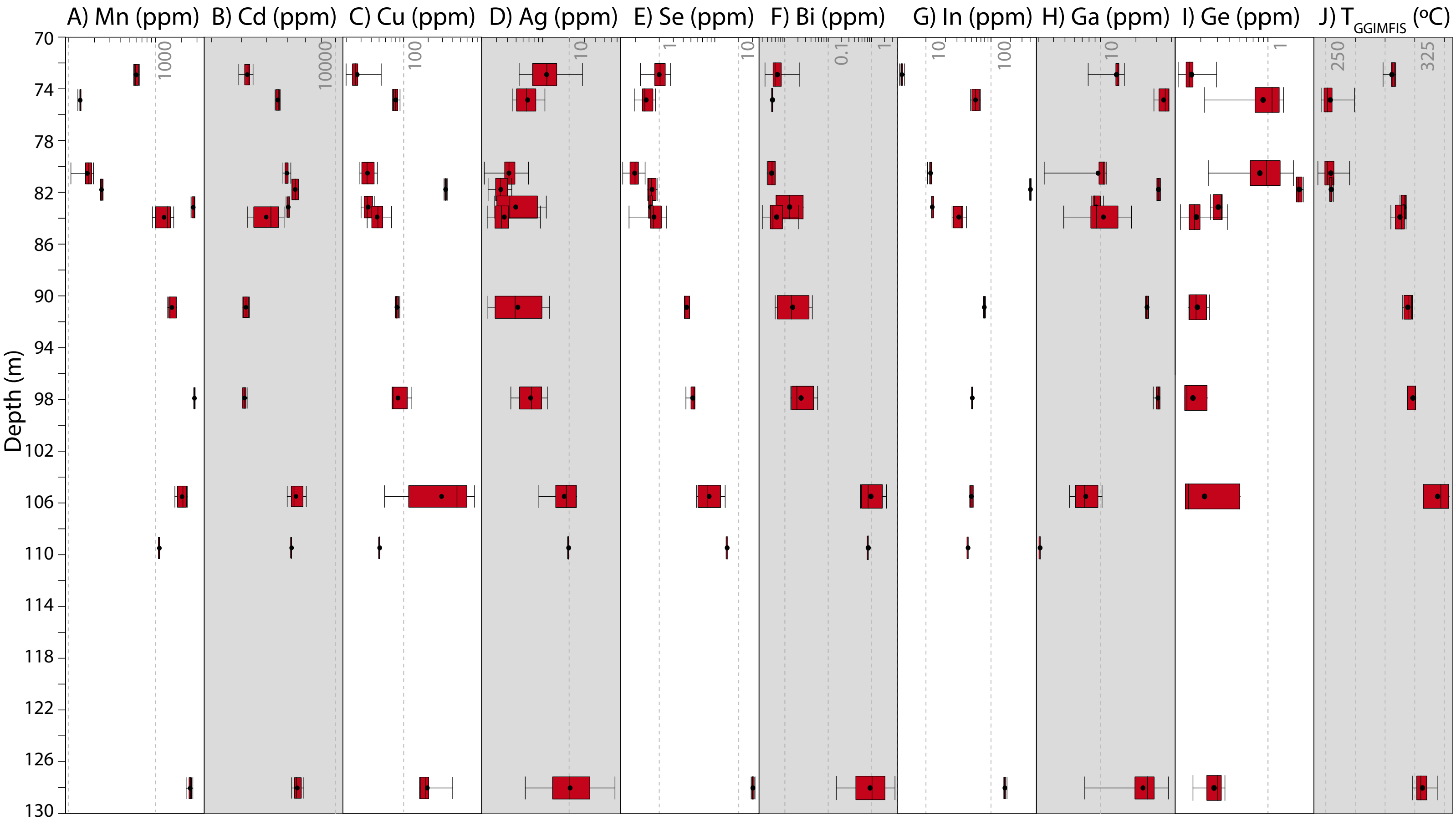

Figure 8

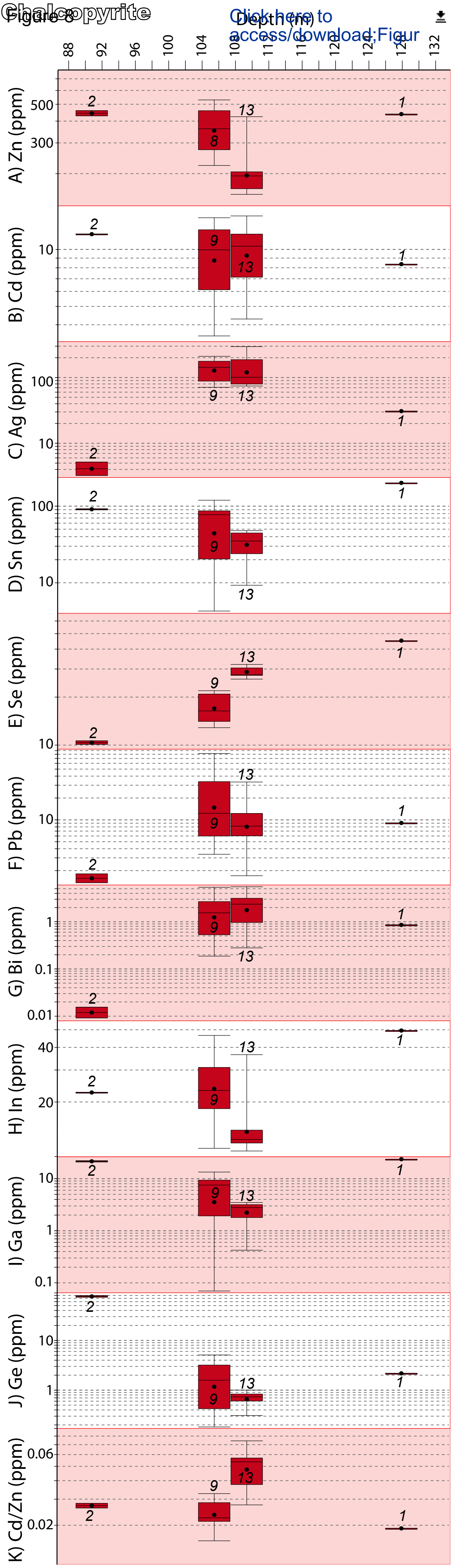
Chalcopyrite
Depth (m)
88
92
96
100
104
108
112
116
120
124
128
132
A) Zn (ppm)
500
300
2
8
13
1
B) Cd (ppm)
10
2
9
13
1
C) Ag (ppm)
100
10
9
13
1
2
D) Sn (ppm)
100
10
2
9
13
1
E) Se (ppm)
10
13
9
2
1
F) Pb (ppm)
10
13
9
2
1
G) Bi (ppm)
1
0.1
0.01
9
13
2
1
H) In (ppm)
40
20
2
9
13
1
I) Ga (ppm)
10
1
0.1
2
9
13
1
J) Ge (ppm)
10
1
2
9
13
1
K) Cd/Zn (ppm)
0.06
0.02
9
13
2
1

Figure 9

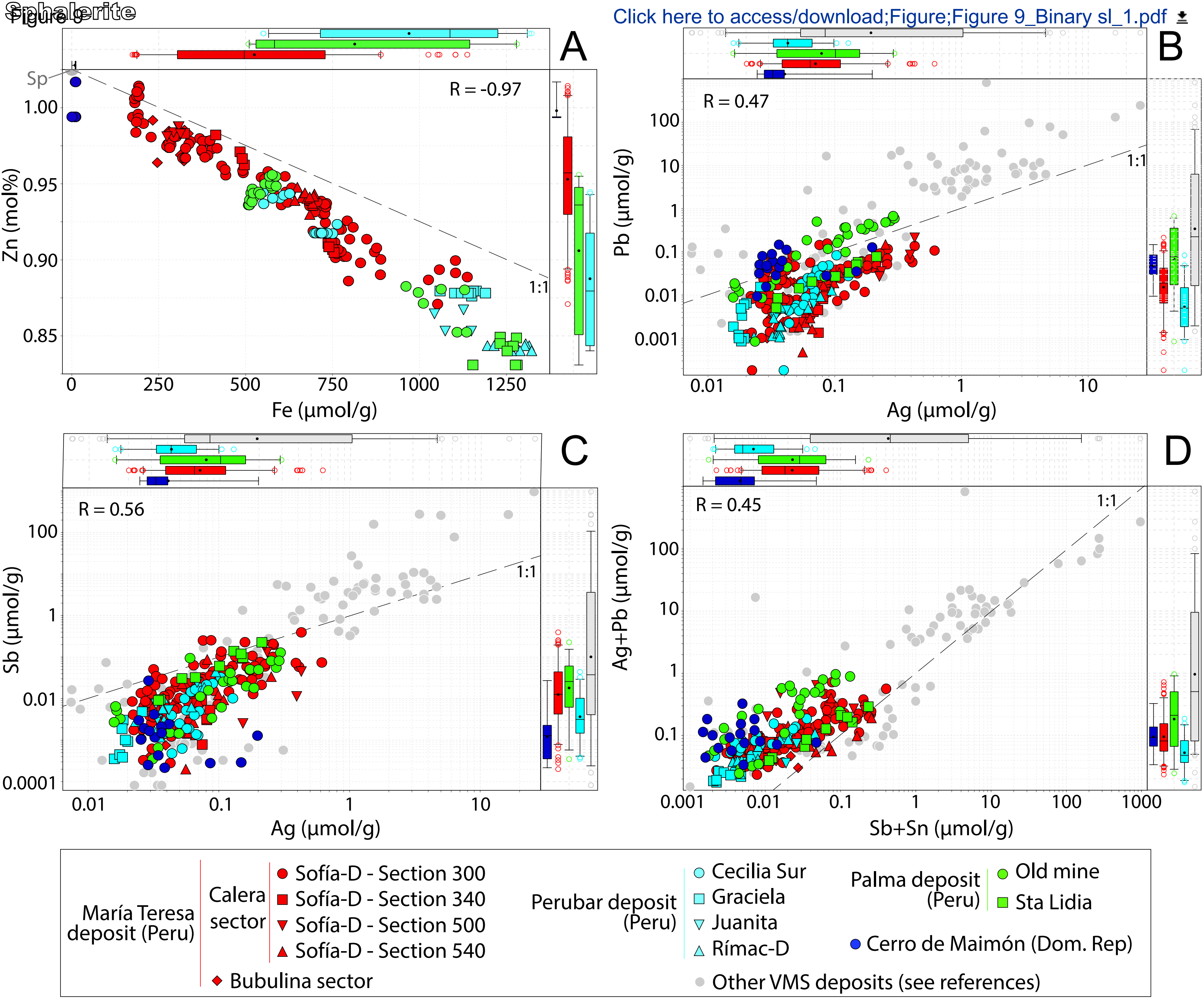
Sphalerite
A
Sp
R = -0.97
1:1
Zn (mol%)
1.00
0.95
0.90
0.85
0
250
500
750
1000
1250
Fe (µmol/g)
B
R = 0.47
1:1
Pb (µmol/g)
100
10
1
0.1
0.01
0.001
0.01
0.1
1
10
Ag (µmol/g)
C
R = 0.56
1:1
Sb (µmol/g)
100
1
0.01
0.0001
0.01
0.1
1
10
Ag (µmol/g)
D
R = 0.45
1:1
Ag+Pb (µmol/g)
100
10
1
0.1
0.001
0.01
0.1
1
10
100
1000
Sb+Sn (µmol/g)
María Teresa deposit (Peru)
Calera sector
● Sofía-D - Section 300
■ Sofía-D - Section 340
▼ Sofía-D - Section 500
▲ Sofía-D - Section 540
◆ Bubulina sector
Perubar deposit (Peru)
○ Cecilia Sur
□ Graciela
▽ Juanita
△ Rímac-D
Palma deposit (Peru)
● Old mine
■ Sta Lidia
● Cerro de Maimón (Dom. Rep)
● Other VMS deposits (see references)

Figure 10

Sphalerite

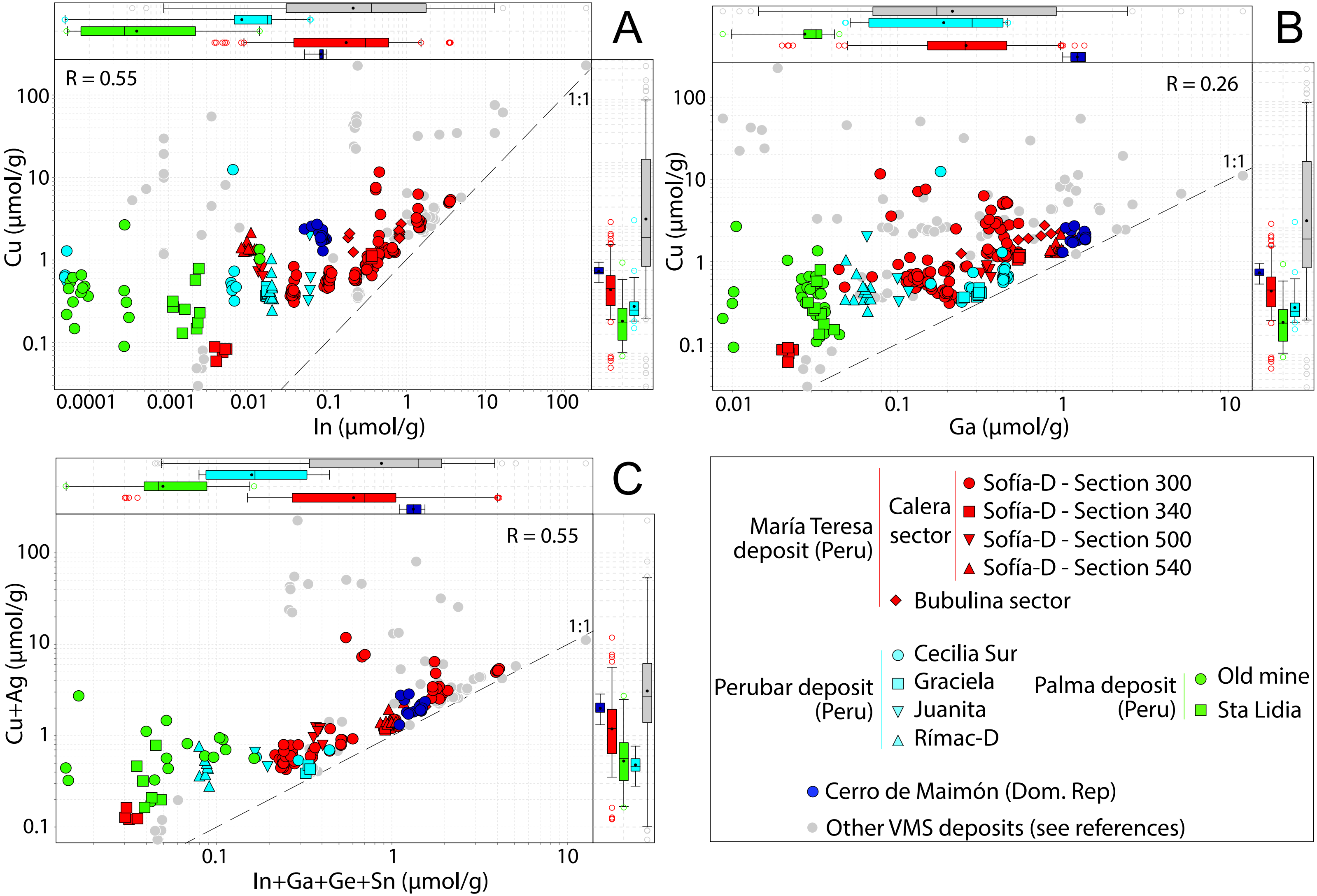

Figure 11

Chalcopyrite

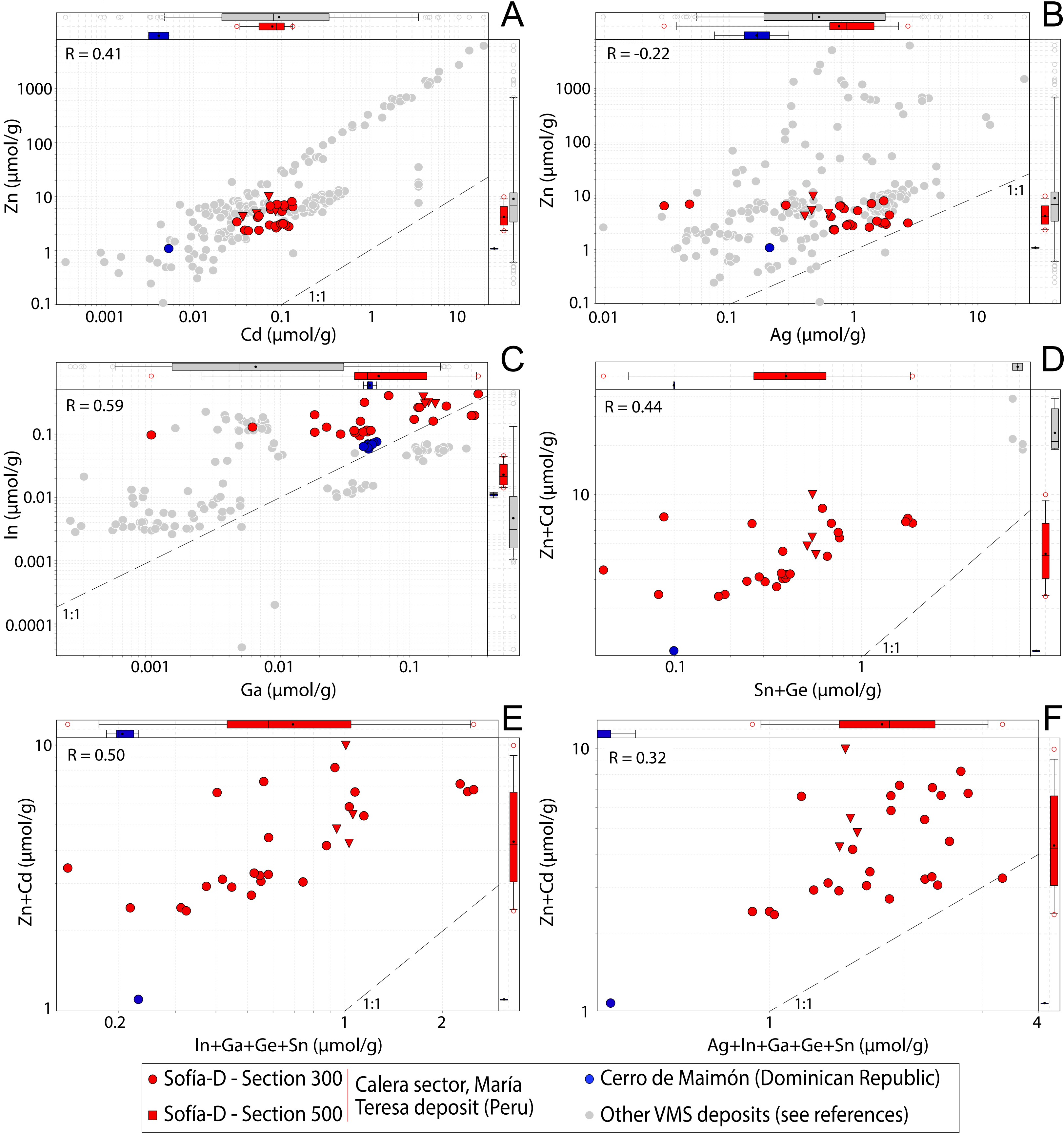

Table 1

Deposit	Sector / Body / Section		Mn (ppm)	Fe (ppm)	Cu (ppm)
María Teresa (Peru)	All samples (n = 141)	Min.	107	9772	3.8
		Max.	4998	63534	740
		GM	1353	29317	96
		SD	1236	13930	106
		IQR	2343-326	40675-17122	98-36
	Bubulina / Bubulina 1180 (n = 9)	Min.	3139	13000	79
		Max.	4998	18702	174
		GM	4474	16628	126
		SD	550	2135	26
		IQR	4747-4492	18088-15614	138-118
	Calera / Sofía-D, all samples (n = 132)	Min.	107	9772	3.8
		Max.	2857	63534	740
		GM	716	26558	61
		SD	939	13984	109
		IQR	1771-303	40842-17173	87-36
	Calera / Sofía-D / 300 (n = 105)	Min.	107	9772	20
		Max.	2857	63534	740
		GM	828	25631	66
		SD	967	14897	120
		IQR	2343-251	42100-15748	90-36
	Calera / Sofía D / 340 (n = 10)	Min.	113	18062	3.8
		Max.	1662	42132	76
		GM	468	31839	19
		SD	799	9365	35
		IQR	1646-139	41573-27114	70-5.3
	Calera / Sofía D / 500 (n = 5)	Min.	320	15296	40
		Max.	584	38233	82
		GM	502	19140	53
		SD	97	8832	15
		IQR	557-520	17392-16548	55-47
	Calera / Sofía D / 540 (n = 12)	Min.	214	35835	82
		Max.	357	38973	137
		GM	322	37824	91
		SD	36	1036	16
		IQR	339-326	38681-37310	89-84
	All samples (n = 50)	min	667	30747	16
		max	7639	73876	789
		GM	2421	51935	35
		SD	2738	15233	108
		IQR	5964-907	67570-39965	41-25
	Cecilia Sur	Min.	667	30747	20

Perubar (Peru)	(n = 22)	Max.	1047	42636	789
		GM	906	37667	45
		SD	75	3821	160
		IQR	939-879	40139-34273	46-36
	Graciela (n = 10)	Min.	6704	59164	23
		Max.	7639	66451	30
		GM	7267	63460	26
		SD	240	2010	2
		IQR	7367-7197	64413-62864	27-24
	Juanita (n = 4)	Min.	1669	58263	20
		Max.	1973	64193	126
		GM	1801	61300	41
		SD	128	2706	49
		IQR	1856-1736	63248-59558	61-25
	Rímac-D (n = 14)	Min.	5121	66771	16
		Max.	6090	73876	66
		GM	5631	71109	27
		SD	325	1984	13
		IQR	5915-5408	72557-70501	30-22
Palma (Peru)	All samples (n = 37)	Min.	2303	28384	5.7
		Max.	10848	71526	170
		GM	6676	42211	20
		SD	2413	17860	29
		IQR	7751-6734	63423-30015	31-11
	Old mine (n = 28)	Min.	2303	28384	5.7
		Max.	7751	63423	170
		GM	5794	35929	21
		SD	1822	12819	33
		IQR	7176-6671	38029-29106	32-12
	Sta Lidia (n = 9)	Min.	9837	64436	8.2
		Max.	10848	71526	50
		GM	10375	69687	17
		SD	332	2237	14
		IQR	10604-10119	71269-68821	44520.0
Cerro de Maimón (Dominican Republic)	Cerro de Maimón (n = 17)	Min.	406	B.D.L.	82
		Max.	539	643	172
		GM	467	371	124
		SD	40	193	22
		IQR	482-446	585-535	138-113

B.D.L.: Below detection limit; IQR: interquartile range; GM: geometric mean; SD: standar

*Ragged ablation spectra in some analyses indicate that these elements may occur as su

** According to Zn concentrate analyses, Cd values (LA-ICP-MS data) may be overevalua

Zn (ppm)	Ga (ppm)	Ge (ppm)	As (ppm)	Se (ppm)	Mo (ppm)	Ag (ppm)
569500	1.4	B.D.L.	4.6	B.D.L.	B.D.L.	2.2
663300	94	2.3	9.3	32	1.6	66
623168	25	0.51	6.0	6.4	0.16	11
22726	19	0.56	0.8	9.3	0.19	10
641300-608100	32-11	0.65-0.17	6.5-5.5	5.3-1.6	0.20-0.047	12-4.2
630300	17	B.D.L.	4.7	4.3	0.25	3.2
648500	94	0.16	5.8	5.3	0.73	5.2
640091	51	0.16	5.3	4.8	0.37	4.2
6640	23	-	0.3	0.4	0.15	0.7
643900-633600	68-43	0.16-0.16	5.4-5.1	5.0-4.6	0.36-0.31	4.6-3.8
569500	1.4	B.D.L.	4.6	B.D.L.	B.D.L.	2.2
663300	70	2.3	9.3	32	1.6	66
621589	17	0.33	6.0	3.1	0.09	7.9
22982	17	0.56	0.8	9.6	0.18	10.6
639625-605100	31-11	0.66-0.17	6.5-5.5	5.5-1.5	0.17-0.045	13-4.2
569500	3.1	B.D.L.	5.2	B.D.L.	B.D.L.	2.2
663300	38	2.3	9.3	32	1.6	66
621999	15	0.37	6.1	3.3	0.11	7.5
24203	10	0.60	0.7	10.6	0.19	10.5
639600-602500	27-10	0.79-0.17	6.4-5.7	5.6-1.5	0.20-0.050	13-3.9
591600	1.4	B.D.L.	6.7	B.D.L.	B.D.L.	4.1
642900	38	0.21	7.1	7.1	0.13	9.2
614743	8	0.16	6.9	3.1	0.06	6.9
22717	19	0.04	0.1	2.8	0.05	1.8
634275-594450	38-1.5	0.19-0.13	7.0-6.9	6.6-1.3	0.11-0.027	8.6-5.7
608000	22	0.12	4.9	1.3	0.033	11
645800	59	0.95	5.6	3.7	0.61	46
637688	28	0.37	5.3	2.1	0.07	24
14717	14	0.31	0.2	0.9	0.23	14
645150-641800	25-24	0.64-0.29	5.4-5.3	2.4-1.7	0.065-0.038	38-18
608000	58	B.D.L.	4.6	2.1	0.037	5.7
619700	70	1.2	5.4	3.7	0.67	27
614685	64	0.22	5.0	2.8	0.06	8.9
2950	4	0.33	0.3	0.4	0.18	6.2
616125-613700	68-63	0.23-0.16	5.2-4.9	3.0-2.6	0.055-0.042	11-6.5
549400	3.4	B.D.L.	4.0	B.D.L.	0.046	1.7
617700	33	0.49	6.1	10	0.55	14
579909.2969	13	0.17	4.6	3.5	0.19	4.6
24068.28288	11	0.08	0.4	3.0	0.17	2.7
600000-551800	30-4.7	0.19-0.15	4.8-4.4	8.2-2.5	0.42-0.089	7.1-3.6
599800	11	B.D.L.	4.3	B.D.L.	0.046	4.3

617700	33	0.19	5.4	4.4	0.20	14
605057	25	0.16	4.7	1.7	0.085	6.8
7381	7	0.03	0.3	1.3	0.031	2.2
614400-600000	31-20	0.17-0.14	4.8-4.6	3.2-1.1	0.098-0.071	7.8-5.7
572900	17	B.D.L.	4.0	3.2	0.39	1.7
575100	22	0.20	4.7	4.2	0.55	2.8
574430	21	0.18	4.3	3.7	0.48	2.0
699	2	0.01	0.2	0.3	0.04	0.3
575100-574200	22-21	0.19-0.18	4.3-4.2	4.0-3.5	0.49-0.46	2.1-1.9
557900	4.5	B.D.L.	4.7	2.5	0.12	3.6
567000	8.1	0.49	6.1	3.9	0.17	7.4
562010	6.5	0.25	5.2	3.1	0.14	4.6
4813	1.5	0.26	0.6	0.6	0.03	1.8
565725-557900	7.4-6.4	0.40-0.22	5.4-5.0	3.3-2.9	0.16-0.12	5.2-3.6
549400	3.4	B.D.L.	4.4	6.5	0.33	2.5
552400	4.8	0.22	4.9	10	0.45	10
551092	4.2	0.17	4.6	8.6	0.38	4.4
1010	0.5	0.03	0.2	1.1	0.04	2.1
551600-550625	4.6-4.0	0.20-0.15	4.8-4.6	9.3-8.3	0.42-0.35	4.1-3.9
543300	0.61	B.D.L.	3.6	B.D.L.	0.13	1.7
625100	3.1	9.3	6.3	1.6	0.69	32
591619	1.9	0.6	4.9	0.94	0.44	8.5
31430	0.6	2.6	0.7	0.25	0.15	8.8
619200-557400	2.4-1.9	3.5-0.16	5.3-4.3	1.1-0.8	0.58-0.41	17-3.8
557400	0.61	B.D.L.	3.6	B.D.L.	0.13	1.7
625100	3.1	9.3	6.3	1.6	0.58	32
605878	1.8	0.9	4.8	1.0	0.39	8
22214	0.7	2.7	0.84	0.29	0.12	10
620375-603350	2.4-1.8	4.6-0.18	5.6-4.0	1.2-0.8	0.47-0.39	18-3.6
543300	2.0	B.D.L.	4.7	B.D.L.	0.64	3.7
555300	2.9	0.23	5.3	1.1	0.69	23
549369	2.3	0.16	5.1	0.86	0.66	9.3
4919	0.2	0.04	0.2	0.12	0.02	6.7
552500-543300	2.4-2.2	0.19-0.14	5.3-4.9	0.9-0.8	0.67-0.64	16-5.6
650000	70	0.23	3.6	17	B.D.L.	2.6
665000	96	6.2	10	67	1.7	21
652622	85.2	0.9	4.4	49	0.20	4.4
5894	9.0	1.4	1.6	17	0.52	5.3
650000-650000	95-78	1.2-0.68	4.4-3.9	61-57	0.30-0.090	4.2-3.1

d deviation

b-microinclusions

ted by 48-57%

Cd (ppm)	In (ppm)	Sn (ppm)*	Sb (ppm)	Hg (ppm)	Tl (ppm)*	Pb (ppm)*
4720	0.44	0.14	B.D.L.	98	B.D.L.	0.038
9409	415	20	48	788	19	44
6605**	60	1.2	4.3	392	1.0	6.2
1279	89	2.8	7.2	135	2.1	7.2
7373-5290	68-4.4	0.61-0.25	5.2-0.52	448-326	1.2-0.060	8.7-1.4
4720	21	0.30	0.048	664	B.D.L.	0.21
5044	99	3.2	1.1	788	0.0081	4.3
4867	59	1.0	0.28	724	0.0067	1.2
118	36	1.0	0.37	35	0.0010	1.7
4964-4804	94-25	1.7-0.35	0.54-0.15	737-704	0.0076-0.0061	4.1-0.62
4896	0.44	0.14	B.D.L.	98	B.D.L.	0.038
9409	415	20	48	677	19	44
6613	19	0.48	1.7	349	0.28	3.4
1235	91	2.86	7.3	107	2.18	7.3
7411-5446	54-4.3	0.58-0.24	5.5-0.65	438-318	1.3-0.084	8.8-1.6
4896	3.9	0.14	B.D.L.	98	0.0072	0.038
8051	415	16	48	485	19	33
6334	33	0.37	2.0	345	0.35	3.9
967	98	2.19	7.7	97	2.39	6.5
7239-5290	78-12	0.48-0.22	5.9-0.79	438-315	1.7-0.13	9.0-2.0
5592	0.44	0.18	0.10	213	B.D.L.	0.28
7044	42	1.8	1.1	443	0.32	2.5
6198	5	0.46	0.40	300	0.05	0.83
656	22	0.45	0.39	105	0.12	0.74
6899-5632	42-0.56	0.58-0.29	0.87-0.24	409-219	0.17-0.019	1.5-0.48
8905	1.1	0.34	0.31	329	0.085	3.9
9409	1.8	2.2	24	677	0.71	44
9121	1.6	0.95	3.3	574	0.23	10
166	0.2	0.71	9.6	130	0.24	15
9152-9054	1.7-1.6	1.6-0.64	13-1.4	654-620	0.44-0.12	16-6.0
8644	1.0	0.61	0.02	325	0.014	0.10
9168	1.5	20	11	356	1.2	31
8877	1.2	3.1	0.9	338	0.14	1.7
158	0.2	5.6	4.0	11	0.45	8.6
8951-8784	1.2-1.1	8.4-1.1	3.1-0.28	344-331	0.38-0.052	4.7-0.45
3977	0.0056	0.17	B.D.L.	15	B.D.L.	0.038
7076	7.1	1.4	5.4	117	1.0	17
5252	1.0	0.27	0.45	44	0.05	1.1
1070	1.8	0.17	1.15	39	0.18	3.3
6664.9-4296.6	2.3-0.78	0.31-0.22	1.2-0.18	107-18	0.13-0.025	2.9-0.39
5485	0.0056	0.20	B.D.L.	71	0.013	0.038

7076	0.82	0.43	4.0	117	1.0	17
6422	0.10	0.31	0.6	97	0.10	2.5
518	0.39	0.07	1.1	16	0.23	4.1
6797-5833	0.75-0.0060	0.35-0.26	1.9-0.23	108-79	0.20-0.047	5.8-1.2
4799	1.9	0.17	B.D.L.	37	0.045	0.18
5135	2.1	0.23	0.59	43	0.17	3.2
4983	2.0	0.20	0.13	40	0.076	0.56
89	0.0	0.02	0.20	2	0.043	0.93
5039-4952	2.0-2.0	0.21-0.19	0.27-0.053	41-39	0.10-0.055	1.2-0.22
3977	6.7	0.19	0.38	15	0.0060	0.63
4388	7.1	1.4	3.0	17	0.49	1.3
4208	6.9	0.35	0.91	16	0.05	0.83
185	0.2	0.57	1.19	1	0.23	0.31
4341-4110	7.0-6.9	0.56-0.20	1.4-0.59	17-16	0.18-0.031	1.0-0.64
3996	2.1	0.19	0.14	17	B.D.L.	0.22
4436	2.4	0.36	5.4	20	0.12	2.7
4235	2.3	0.25	0.47	18	0.011	0.52
104	0.1	0.04	1.40	1	0.034	0.73
4291-4185	2.3-2.2	0.27-0.22	0.75-0.20	19-18	0.028-0.0044	1.0-0.26
4335	0.0059	0.15	B.D.L.	213	B.D.L.	0.17
7951	1.6	0.90	28	1215	6.2	140
5703	0.046	0.30	2.2	603	0.2	14
1212	0.421	0.16	6.2	316	1.4	42
7109-4782	0.22-0.0091	0.41-0.20	7.1-0.78	667-593	1.4-0.020	71-3.9
4335	0.0059	0.15	B.D.L.	213	B.D.L.	0.17
7293	1.6	0.63	16	667	6.2	140
5227	0.0	0.27	2	487	0.3	19
848	0.52	0.14	4.1	166	1.5	44
5382-4742	0.032-0.0072	0.36-0.18	5.8-0.47	621-504	1.7-0.034	77-4.5
7109	0.13	0.26	1.1	1147	0.0056	1.1
7951	0.28	0.90	28	1215	0.21	16
7481	0.21	0.40	6.1	1169	0.034	5.0
251	0.06	0.19	8.8	21	0.070	5.1
7647-7315	0.27-0.17	0.42-0.33	15-3.7	1177-1156	0.11-0.018	10-3.0
3413	5.9	0.14	0.026	21	0.036	1.9
3905	11	2.5	3.3	30	1.51	30
3684	9.5	0.37	0.15	23.8	0.15	9.9
146	1.3	0.60	0.77	2.9	0.38	8.2
3829-3574	10-9.5	0.50-0.23	0.26-0.052	26-22	0.23-0.061	17-6.6

Bi (ppm)*
B.D.L.
3.5
0.44
0.77
0.60-0.0055
B.D.L.
B.D.L.
B.D.L.
B.D.L.
B.D.L.
B.D.L.
3.46
0.04
0.77
0.60-0.0055
B.D.L.
3.5
0.053
0.801
0.72-0.0057
B.D.L.
0.0051
0.0046
0.0006
0.0050-0.0044
B.D.L.
0.0061
0.0061
-
0.0061-0.0061
B.D.L.
0.011
0.0069
0.0035
0.0084-0.0053
B.D.L.
0.0037
0.0033
0.0005
0.0035-0.0031
B.D.L.

B.D.L.
B.D.L.
B.D.L.
B.D.L.
B.D.L.
B.D.L.
B.D.L.
B.D.L.
B.D.L.
B.D.L.
B.D.L.
B.D.L.
B.D.L.
B.D.L.
B.D.L.
0.0037
0.0033
0.0005
0.0035-0.0031
B.D.L.
0.015
0.004
0.006
0.0066-0.0025
B.D.L.
0.015
0.005
0.007
0.0089-0.0025
B.D.L.
0.0037
0.0037
-
0.0037-0.0037
0.054
3.5
0.5
1.0
1.1-0.33

Table 2

Deposit	Sector/Body/Section		Fe (ppm)	Co (ppm)	Ni (ppm)
María Teresa (Peru)	All samples (n = 40)	Min.	264304	B.D.L.	B.D.L.
		Max.	373972	0.087	2.2
		GM	331188	0.075	1.5
		SD	24272	0.010	0.4
		IQR	348538-319792	0.079-0.070	1.9-1.2
	Calera / Sofía D / 300 (n = 25)	Min.	264304	B.D.L.	B.D.L.
		Max.	373972	0.087	2.2
		GM	331249	0.075	1.4
		SD	25625	0.010	0.4
		IQR	348538-319792	0.079-0.070	1.8-1.2
	Calera / Sofía D / 500 (n = 4)	Min.	312109	B.D.L.	B.D.L.
		Max.	350244	B.D.L.	1.9
		GM	330803	-	1.9
		SD	15609	-	0.1
		IQR	336816-325247	-	1.9-1.8
Cerro de Maimón (Dominican Republic)	Cerro de Maimón (n = 11)	Min.	270450	1.2	B.D.L.
		Max.	316435	3.1	2.5
		GM	296657	1.8	1.7
		SD	14668	0.6	0.4
		IQR	307234-285613	2.0-1.5	1.9-1.5

B.D.L.: Below detection limit; IQR: interquartile range; GM: geometric mean; SD: standa

*Ragged ablation spectra indicate that these elements may occur as sub-microinclusior

Cu (ppm)	Zn (ppm)	Ga (ppm)	Ge (ppm)	As (ppm)	Se (ppm)	Mo (ppm)*	Ag (ppm)
340000	152	0.070	0.18	0.18	10	B.D.L.	3.2
352700	647	24	80	1.9	59	0.044	295
346217	277	4.0	1.6	0.43	25	0.027	82
3871	133	6.4	19.4	0.41	13	0.008	67
348300-343900	425-194	9.2-2.6	4.3-0.66	0.74-0.29	31-19	0.034-0.021	150-71
342000	152	0.070	0.18	0.18	10	B.D.L.	3.2
352700	529	24	80	1.9	45	0.044	295
347222	263	3.5	1.2	0.45	22	0.027	89
3155	124	6.8	20.9	0.43	8	0.008	68
349700-345000	425-192	8.1-2.6	2.2-0.64	0.80-0.29	30-16	0.035-0.021	166-76
340000	276	8.9	7.3	0.25	49	B.D.L.	44
340000	647	11	12	0.36	59	0.033	68
340000	374	10	9.4	0.30	53	0.025	52
-	170	1	2.4	0.05	4	0.007	10
340000-340000	425-303	10-9.1	11-7.8	0.33-0.28	54-50	0.028-0.022	55-48
346300	B.D.L.	3.1	4.8	0.36	60	5.4	8.3
346300	71	3.9	6.6	2.0	94	250	33
346300	71	3.4	5.6	0.86	81	40	18
-	-	0.2	0.6	0.54	11	69	7
346300-346300	-	3.6-3.3	6.1-5.3	1.3-0.56	89-79	83-23	23-15

ard deviation

ns

Cd (ppm)	In (ppm)	Sn (ppm)	Sb (ppm)*	Au (ppm)*	Hg (ppm)	Tl (ppm)*	Pb (ppm)*
3.5	11	4.3	1.4	B.D.L.	B.D.L.	0.019	1.4
15	49	201	31	0.40	3.8	11	82
8.8	20	43	6.8	0.069	1.1	0.8	7.8
3.3	12	40	7.3	0.091	1.1	3.0	16.4
12-6.2	32-12	77-33	12-3.2	0.12-0.039	1.9-0.69	2.4-0.28	12-4.3
3.5	11	4.3	1.4	B.D.L.	B.D.L.	0.019	1.4
15	49	201	31	0.40	3.8	11	82
9.2	18	42	6.6	0.077	1.0	0.8	8.8
3.2	11	43	7.4	0.095	0.9	3.2	17.2
12-8.2	23-12	78-30	10-3.2	0.13-0.041	1.5-0.69	2.4-0.28	14-6.0
4.1	34	43	3.6	0.016	0.57	0.62	1.5
9.6	44	53	17	0.075	3.7	3.4	7.9
6.6	37	49	7.8	0.036	1.9	1.7	3.6
2.4	5	4	7.2	0.029	1.5	1.1	3.2
8.4-5.4	38-34	52-47	16-3.8	0.065-0.020	3.5-1.5	2.5-1.5	7.0-1.9
B.D.L.	6.7	1.2	0.05	0.015	B.D.L.	0.026	5.1
0.59	8.7	1.8	0.34	0.13	0.27	0.42	39
0.45	7.7	1.5	0.16	0.043	0.17	0.078	12
0.17	0.6	0.2	0.10	0.034	0.06	0.123	12
0.53-0.41	8.1-7.3	1.6-1.4	0.25-0.10	0.071-0.027	0.21-0.14	0.15-0.042	21-7.1

Bi (ppm)*
0.0092
5.5
1.0
1.6
2.5-0.54
0.0092
5.5
1.0
1.6
2.6-0.86
0.45
2.5
1.0
1.0
1.8-0.52
1.5
10
3.8
3.4
8.0-2.2

Table 3

Deposit	Location	*ppm*	Mn	Fe	Cu
Vorta	Romania	Max	761	2617	719
(n = 8)		Min	165	917	131
		GM	485	1844	334
		SD	201	584	193
		IQR	650-424	2404-1524	475-274
Eskay Creek	Canada	Max	4744	7112	3483
(n = 12)		Min	2296	3880	67
		GM	3206	4814	356
		SD	648	900	1017
		IQR	3437-3113	5284-4316	835-116
Zinkgruvan	Sweden	Max	532	33261	5.1
(n = 5)		Min	499	31735	1.9
		GM	513	32330	3.3
		SD	14	737	1.2
		IQR	524-502	33006-31751	4.0-3.1
Marketorp	Sweden	Max	18729	119418	14368
(n = 8)		Min	1684	86959	1414
		GM	2606	96260	3020
		SD	5930	12125	4246
		IQR	2373-1714	100257-88877	3290-2281
Sauda	Norway	Max	1449	120205	44
(n = 10)		Min	874	69576	22
		GM	959	77585	28
		SD	170	14797	8.6
		IQR	939-903	75796-72800	37-23
Çayeli	NE Turkey	Max	486	182759	210618
(n = 40)		Min	0.35	8.0	65
		GM	22	2857	9638
		SD	102	32933	41584
		IQR	83-5.2	16904-822	35768-6982
Laochang	S China	Max	4111	154203	2020
(n = 30)		Min	2626	121694	119
		GM	3040	130599	211
		SD	364	7814	339
		IQR	3255-2724	137135-125803	254-151

B.D.L.: Below detection limit; n.a.: not analyzed; GM: geometric mean; SD: stan

Ga	Ge	As	Se	Mo	Ag	Cd	In	Sn
363	23	n.a.	1.4	149	21	5088	0.060	0.24
75	2.7	n.a.	0.82	8.0	1.4	4169	0.040	0.050
118	8.0	n.a.	1.1	40	3.7	4734	0.049	0.080
100	7.2	n.a.	0.18	50	6.7	337	0.014	0.072
171-79	12-5.8	n.a.	1.2-1.0	71-20	5.3-2.0	5044-4562	0.055-0.045	0.080-0.055
857	14	1550	4.1	31	2785	4955	14	31
19	0.47	1	1.3	0.15	6.8	2720	0.10	2.6
86	1.2	27	2.1	0.63	102	3796	0.29	9.1
228	3.7	435	1.3	8.7	872	679	3.9	11
123-61	1.4-0.89	196-3.9	3.3-1.5	0.77-0.29	575-15	4394-3294	0.45-0.10	19.8-5.2
2.8	1.2	n.a.	1.9	n.a.	13	3943	0.32	0.25
1.9	0.82	n.a.	1.9	n.a.	4.6	3661	0.26	0.080
2.2	1.1	n.a.	1.9	n.a.	6.0	3811	0.29	0.13
0.38	0.15	n.a.	-	n.a.	3.5	126	0.026	0.077
2.4-1.9	1.2-1.1	n.a.	1.9-1.9	n.a.	6.1-4.6	3933-3718	0.31-0.27	0.21-0.090
9.6	13	n.a.	36	0.68	34	3619	28	0.81
0.61	1.8	n.a.	29	0.11	7.4	2968	25	0.090
1.5	2.7	n.a.	33	0.27	12	3246	26	0.20
3.1	3.7	n.a.	1.8	0.40	8.8	191	1.1	0.26
1.8-0.87	2.6-1.9	n.a.	34-33	0.54-0.25	14-8.7	3304-3135	27-26	0.29-0.13
8.6	1.4	n.a.	109	0.17	5.5	3488	42	1.3
4.1	0.86	n.a.	89	0.17	2.4	1973	27	0.27
5.5	1.0	n.a.	94	0.17	3.7	2170	29	0.56
1.4	0.16	n.a.	6.0	-	1.0	455	4.4	0.38
6.0-4.7	1.1-0.92	n.a.	96-90	0.17-0.17	4.5-3.1	2117-2031	30-28	0.97-0.38
n.a.	n.a.	7261	62	222	450	8957	n.a.	512
n.a.	n.a.	0.19	0.13	0.030	0.80	1051	n.a.	0.43
n.a.	n.a.	345	7.1	5.0	51	3234	n.a.	14
n.a.	n.a.	1874	12	45	98	1936	n.a.	81
n.a.	n.a.	1693-275	13-5.0	18-0.99	138-40	3430-2636	n.a.	44-4.4
117	15	36	4.0	n.a.	10	9600	566	38
2.3	2.1	0.33	0.62	n.a.	4.8	8306	66	2.2
15	3.8	2.2	1.6	n.a.	6.7	8736	184	5.6
24	2.5	9.7	1.1	n.a.	1.3	240	89	6.9
24-8.9	3.9-2.9	4.1-0.93	2.5-1.0	n.a.	7.5-5.9	8853-8562	235-164	7.7-3.9

dard deviation; IQR: interquartile range

Sb	Hg	Tl	Pb	Bi	Reference
17	n.a.	1.1	3426	0.71	Cook et al. (2009)
0.040	n.a.	0.010	0.46	0.020	
1.1	n.a.	0.034	12	0.16	
5.7	n.a.	0.50	1201	0.27	
2.3-0.75	n.a.	0.040-0.010	68-2.1	0.49-0.085	
117467	n.a.	21	50955	0.19	Cook et al. (2009)
5.1	n.a.	0.081	1.2	0.020	
1034	n.a.	0.83	467	0.041	
33692	n.a.	7.1	15639	0.056	
31973-33	n.a.	2.3-0.17	17228-13	0.053-0.028	
4.1	n.a.	n.a.	193	0.15	Cook et al. (2009)
0.12	n.a.	n.a.	1.4	0.060	
0.54	n.a.	n.a.	8.0	0.094	
1.7	n.a.	n.a.	84	0.033	
1.4-0.24	n.a.	n.a.	15-2.8	0.10-0.080	
0.080	n.a.	0.30	29	74	Cook et al. (2009)
0.040	n.a.	0.024	0.81	2.2	
0.057	n.a.	0.072	7.1	13	
0.019	n.a.	0.10	9.6	24	
0.070-0.040	n.a.	0.11-0.045	17-6.5	30-4.3	
0.10	n.a.	n.a.	n.a.	0.99	Cook et al. (2009)
0.010	n.a.	n.a.	n.a.	0.12	
0.018	n.a.	n.a.	n.a.	0.31	
0.035	n.a.	n.a.	n.a.	0.27	
0.020-0.010	n.a.	n.a.	n.a.	0.47-0.18	
3354	n.a.	97	171820	254	Revan et al. (2014)
0.68	n.a.	0.030	8.0	B.D.L.	
141	n.a.	5.2	727	-	
632	n.a.	20	26976	-	
683-52	n.a.	13-4.9	2123-549	113-6.8	
4.1	n.a.	2.6	556	0.050	Ye et al. (2011)
B.D.L.	n.a.	0.0060	0.30	B.D.L.	
-	n.a.	0.19	2.9	-	
-	n.a.	0.61	101	-	
1.6-0.10	n.a.	0.72-0.053	9.2-0.58	0.010-0.010	

Table 4

Deposit	Location	*ppm*	Co	Ni	Zn	Ga	Ge
Vorta	Romania	Min	12	n.a.	199	0.11	n.a.
(n = 8)		Max	12	n.a.	538	2.2	n.a.
		GM	12	n.a.	391	0.71	n.a.
		SD	-	n.a.	130	0.70	n.a.
		IQR	12-12	n.a.	479-395	1.4-0.49	n.a.
Sulitjelma	Norway	Min	0.016	0.049	97	0.017	n.a.
(n = 120)		Max	28	5.1	861	19	n.a.
		GM	0.8	0.42	381	0.43	n.a.
		SD	3.7	1.3	195	4.1	n.a.
		IQR	2.6-0.27	1.0-0.20	569-329	2.3-0.098	n.a.
Çayeli	NE Turkey	Min	0.010	B.D.L.	7.0	n.a.	n.a.
(n = 69)		Max	166	200	407977	n.a.	n.a.
		GM	0.7	-	1305	n.a.	n.a.
		SD	27	-	69136	n.a.	n.a.
		IQR	1.8-0.17	7.0-0.38	30530-56	n.a.	n.a.
Kutlular	NE Turkey	Min	B.D.L.	0.010	70	n.a.	n.a.
(n = 9)		Max	0.90	0.34	5891	n.a.	n.a.
		GM	-	0.037	304	n.a.	n.a.
		SD	-	0.14	1885	n.a.	n.a.
		IQR	0.26-0.010	0.21-0.010	751-98	n.a.	n.a.

B.D.L.: Below detection limit; n.a.: not analyzed; GM: geometric mean; SD: standard deviat

As	Se	Mo	Ag	Cd	In	Sn	Sb	Au
2.8	n.a.	n.a.	18	0.48	0.0049	0.19	0.11	0.0080
5.8	n.a.	n.a.	92	3.2	0.76	0.79	5.6	0.034
4.1	n.a.	n.a.	45	1.6	0.044	0.39	2.0	0.021
1.3	n.a.	n.a.	23	1.0	0.43	0.28	1.8	0.012
5.2-3.2	n.a.	n.a.	55-41	2.2-1.3	0.39-0.014	0.73-0.23	3.8-2.8	0.033-0.019
1.2	4.4	n.a.	5.1	0.79	0.301	0.091	0.025	0.0031
5.3	926	n.a.	331	58	26	75	15	0.76
2.4	101	n.a.	71	10	2.1	4.6	0.7	0.032
1.1	267	n.a.	95	16	6.1	26	3.7	0.14
3.4-1.7	202-51	n.a.	201-32	29-3.1	6.7-0.61	51-0.43	2.0-0.18	0.088-0.013
B.D.L.	3.6	0.11	4.0	0.040	n.a.	1.1	B.D.L.	B.D.L.
5008	408	290	2549	2194	n.a.	96	3524	25
-	62	15	46	12	n.a.	15	-	-
-	124	65	375	366	n.a.	24	-	-
656-5.6	225-17	54-4.6	132-12	163-1.3	n.a.	39-8.4	117-2.2	0.64-0.063
1.7	220	0.010	1.1	0.67	n.a.	9.1	0.50	0.030
20	340	2223	45	33	n.a.	31	7.8	1.3
5.4	281	7.7	6.8	2.7	n.a.	18	1.4	0.17
5.4	46	795	18	10	n.a.	7.1	2.5	0.48
7.3-2.8	334-258	265-0.20	7.0-4.14	5.6-0.99	n.a.	22-15	1.4-0.82	0.21-0.090

ion; IQR: interquartile range

Hg	Tl	Pb	Bi	Reference
0.34	0.014	6.1	0.010	George et al. (2018)
2.6	0.17	53	2.2	
0.62	0.068	14	0.075	
0.82	0.061	26	1.3	
0.82-0.38	0.14-0.058	30-7.1	1.1-0.015	
0.051	0.0016	0.071	0.019	George et al. (2018)
0.74	3.0	28	11	
0.20	0.015	0.93	0.41	
0.17	0.50	5.4	2.2	
0.32-0.12	0.089-0.0036	1.7-0.37	0.89-0.15	
n.a.	0.010	4.0	0.030	Revan et al. (2014)
n.a.	243	244075	1000	
n.a.	1.2	307	35	
n.a.	38	30588	217	
n.a.	14-0.14	1813-43	170-7.0	
n.a.	0.020	5.0	16	Revan et al. (2014)
n.a.	6.6	494	1764	
n.a.	0.21	37	93	
n.a.	2.5	186	587	
n.a.	0.59-0.030	55-16	94-50	

Figure S1

Figure S2

Figure S3

Table S1

Click here to access/download

Supplementary Material

Table S1_Samples VMS.xlsx

Table S2

Table S3

Click here to access/download
Supplementary Material
Table S3_LAdata.xlsx